Extended virtual element method for the Laplace problem with singularities and discontinuities

E. Benvenuti[a], A. Chiozzi[a,*], G. Manzini[b], N. Sukumar[c,*]

[a] *Department of Engineering, University of Ferrara, Via Saragat 1, 44122 Ferrara, Italy*
[b] *Group T-5, Theoretical Division, Los Alamos National Laboratory, Los Alamos, NM 87545, USA*
[c] *Department of Civil and Environmental Engineering, University of California, Davis, CA 95616, USA*

Abstract

In this paper, we propose the extended virtual element method (X-VEM) to treat singularities and crack discontinuities that arise in the Laplace problem. The virtual element method (VEM) is a stabilized Galerkin formulation on arbitrary polytopal meshes, wherein the basis functions are implicit (virtual)—they are not known explicitly nor do they need to be computed within the problem domain. Suitable projection operators are used to decompose the bilinear form on each element into two parts: a consistent term that reproduces the first-order polynomial space and a correction term that ensures stability. A similar approach is pursued in the X-VEM with a few notable extensions. To capture singularities and discontinuities in the discrete space, we augment the standard virtual element space with an additional contribution that consists of the product of virtual nodal basis (partition-of-unity) functions with enrichment functions. For discontinuities, basis functions are discontinuous across the crack and for singularities a weakly singular enrichment function that satisfies the Laplace equation is chosen. For the Laplace problem with a singularity, we devise an extended projector that maps functions that lie in the extended virtual element space onto linear polynomials and the enrichment function, whereas for the discontinuous problem, the consistent element stiffness matrix has a block-structure that is readily computed. An adaptive homogeneous numerical integration method is used to accurately and efficiently (no element-partitioning is required) compute integrals with integrands that are weakly singular. Once the element projection matrix is computed, the same steps as in the standard VEM are followed to compute the element stabilization matrix. Numerical experiments are performed on quadrilateral and polygonal (convex and nonconvex elements) meshes for the problem of an *L*-shaped domain with a corner singularity and the problem of a cracked membrane under mode III loading, and results are presented that affirm the sound accuracy and demonstrate the optimal rates of convergence in the L^2 norm and energy of the proposed method.

Keywords: virtual element method; partition-of-unity enrichment; X-VEM; crack discontinuity; vertex singularity; polygonal meshes

*Corresponding authors
  Email addresses: `andrea.chiozzi@unife.it` (A. Chiozzi), `nsukumar@ucdavis.edu` (N. Sukumar)

1. Introduction

Over the past two decades, enriched approximations based on the partition-of-unity framework proposed by Melenk and Babuška [1, 2] have been adopted to model physical phenomena that admit discontinuities and singularities within the problem domain. An instance of the partition-of-unity finite element method is the extended finite element method (X-FEM) [3], which has become an attractive choice to conduct elastic fracture simulations on finite element meshes without the need for extensive remeshing. In this paper, we develop a new numerical formulation that leads to mesh-independent modeling on polygonal meshes and improved numerical approximation for Laplace problems that have discontinuous and/or weakly singular solutions by generalizing concepts from the X-FEM to the virtual element method (VEM). Among the methods for fracture on polygonal meshes that are germane to the present study, we mention the X-FEM [4], polygonal finite elements [5] and the scaled boundary finite element method [6]. In contrast to these approaches, we devise a method that is efficient, provides flexibility, and is simpler to implement. Notably, shape functions on general (convex and nonconvex) polygons are not required to be known, and furthermore, we use the homogeneous numerical integration (HNI) method [7, 8] to compute the weak form integrals without the need to partition the elements in the mesh.

The VEM, originally proposed in Beirão da Veiga et al. [9], is a recent development in stable Galerkin discretizations on polytopal meshes to solve boundary-value problems. In the VEM, the basis functions are defined as the solution of a local elliptic partial differential equation, and are never explicitly computed in the implementation of the method. For this reason, they are dubbed as *virtual*, and the finite element space of the VEM as the *virtual element space*. Since the virtual basis functions are unknown, the VEM uses their elliptic polynomial projections to build the bilinear form (stiffness matrix) and the continuous linear functional (forcing or loading term) of the variational formulation. Such projections are computable from the degrees of freedom without introducing any further approximation error and are used to decompose the bilinear form on each element into two parts: the consistent term that approximates the stiffness matrix on a given polynomial space and the correction term that ensures stability. As in the finite element method (FEM), element-level assembly procedures are used to obtain the discrete system of linear equations.

On nonsmooth domains and in the presence of nonsmooth data, the solution of elliptic problems such as the Poisson or Laplace equations may contain weak singularities [10] that worsen the convergence rate of any numerical method that assumes a more regular approximate solution, such as the FEM, and *a fortiori*, the VEM. In such a case, it may be beneficial to augment the finite element space defined on the elements that are proximal to the singularity by introducing additional set of basis functions. These basis functions are built upon suitable *enrichment functions*, which are carefully chosen to mimic the properties of the aforementioned singularity. In doing so, some information about the exact solution is incorporated (for instance via the framework of partition-of-unity) into the computational method, thus removing, or at least alleviating, the effect of the singularity on the scheme's accuracy. This forms the basis of enriched partition-of-unity methods and the X-FEM in particular, and herein we refer to the proposed approach as the *eXtended VEM* (X-VEM). In principle, any number of auxiliary functions can be considered to enrich the virtual element space according to the problem at hand—to solve the Helmholtz problem, Perugia et al. [11] were the first to introduce approximating spaces that

consist of the product of low-order virtual element basis functions and a planewave (nonpolynomial, smooth function) in each direction. For simplicity and in the interest of clarity, in this study we only consider one enrichment function in the extended virtual element solution of the Laplace boundary-value problem.

Since the inception of the VEM [9, 12, 13], there have only been a few contributions that leverage the flexibility of the method to construct admissible approximations on finite element meshes that are cut by a strong or weak discontinuity. Notable among these are the use of VEM to simulate flow in discrete fracture networks [14, 15], modeling of zero-thickness interface elements for fracture in heterogeneous materials [16], and the application of the VEM to 2D elastic fracture simulations [17]. In these contributions, nodes are inserted at locations where each interface intersects an element, which results in the partitioning of a finite element into a collection of polygonal elements. Two such elements have so-called *hanging nodes* on the common edge that lie on the material interface (weak discontinuity), but the VEM approximation is, however, C^0-conforming along the edge [15], whereas the nodes that lie on a traction-free crack in elastic media are duplicated (similar to the FEM) to represent a discontinuous field [17].

The outline of the remainder of this article follows. In Section 2, we present the strong and weak forms of the Laplace boundary-value problem. In Section 3, we describe the extended virtual element formulation. For the Laplace problem with a singularity, we devise an extended projector that maps functions that lie in the extended virtual element space onto linear polynomials and the enrichment function. For a discontinuity that cuts an element, instead of enriching with a discontinuous function through the partition-of-unity framework as is done in the X-FEM, we adopt the approach of Hansbo and Hansbo [18], whereby each virtual shape function is decomposed as the sum of two discontinuous shape functions. It is known that the approximation in the X-FEM and the approach of Hansbo and Hansbo [18] are equivalent [19]. The consistent element stiffness matrix so formed has a block-structure that is readily computed. In Section 4, we provide a detailed description of how the method is implemented. In Section 5, we first compare the accuracy of product Gauss cubature scheme to the HNI method [7] for the evaluation of the weak form integrals. Then, we present two applications of the X-VEM on polygonal meshes: the problem of the *L*-shaped domain with a corner singularity and the solution of the Laplace crack problem. A discontinuous patch test [20] for the Laplace crack problem is solved to verify the consistency of the formulation. We solve the *L*-shaped domain problem using geometric enrichment and the mode III crack problem, and show that the method delivers optimal rates of convergence in the L^2 norm and the strain energy. Finally, we close with some final remarks in Section 6.

2. Strong and weak forms of Laplace problem

Let $\Omega \subset \mathbb{R}^2$ be an open, bounded domain with Lipschitz continuous boundary Γ. We consider the following Laplace boundary-value problem:

$$\Delta u = 0 \qquad \text{in } \Omega, \tag{1a}$$

$$u = g_D \qquad \text{on } \Gamma_D, \tag{1b}$$

$$\boldsymbol{n} \cdot \nabla u = g_N \qquad \text{on } \Gamma_N, \tag{1c}$$

where u is the scalar unknown, $\Gamma = \overline{\Gamma}_D \cup \overline{\Gamma}_N$ and $\Gamma_D \cap \Gamma_N = \emptyset$ with Γ_D and Γ_N representing the Dirichlet and Neumann boundaries, respectively, and g_D and g_N are the boundary data on Γ_D

3

and Γ_N, respectively.

Let $V = H^1_{g_D}(\Omega)$ denote the affine subspace of functions in the Sobolev space $H^1(\Omega)$ whose trace on Γ_D is equal to g_D, and $V_0 \subset V$ the linear subspace of functions that are zero on Γ_D. The variational formulation of problem (1a)-(1c) reads as: find $u \in V$ such that

$$a(u, v) = (g_N, v)_{\Gamma_N} \quad \forall v \in V_0, \tag{2}$$

where the bilinear form $a(\cdot, \cdot)$ and the linear functional $(\cdot, \cdot)_{\Gamma_N}$ are given by

$$a(u, v) = \int_\Omega \nabla u \cdot \nabla v \, d\boldsymbol{x}, \quad (g_N, v)_{\Gamma_N} = \int_{\Gamma_N} g_N v \, ds, \quad u \in V, \ v \in V_0. \tag{3}$$

The Dirichlet boundary condition in (1b) is incorporated in the definition of the functional space V. The Neumann boundary condition in (1c) is expressed by $(\cdot, \cdot)_{\Gamma_N}$ in (3). When Γ_D in nonempty and under suitable regularity assumptions on g_D and g_N, the exact solution to problem (2) exists and is unique. This result is a consequence of the coercivity and continuity of $a(\cdot, \cdot)$ and the Lax-Milgram lemma.

Remark 2.1. *Here we consider the Laplace problem for the sake of simplicity, but the case of a non-homogeneous right-hand side is readily handled in the standard VEM, cf. [9, 12, 13].*

3. Extended virtual element formulation

From the weak form of the continuous problem in (2), we can write the weak form for the X-VEM as: find $u^h_X \in V^h_{X,g_D} \subset V$ such that

$$a_h(u^h_X, v^h_X) = \left(g_N, v^h_X\right)_{\Gamma_N, h} \quad \forall v^h_X \in V^h_{X,0} \subset V_0, \tag{4}$$

where $a_h(\cdot, \cdot)$ and $(\cdot, \cdot)_{\Gamma_N, h}$ are the virtual element bilinear form and the continuous linear functional that approximate the exact bilinear form $a(\cdot, \cdot)$ and $(\cdot, \cdot)_{\Gamma_N}$ in the enriched setting. Spaces V^h_{X,g_D} and $V^h_{X,0}$ are built from the enrichment of the finite-dimensional virtual element space V^h, which is a conforming subspace of V, and provides the enriched virtual element space V^h_X. The well-posedness of (4) follows from the coercivity and continuity of the bilinear form a_h on V^h_X, which is proved later in this section.

For now, let $\{\phi_i\}^N_{i=1}$ be the canonical basis functions in the X-VEM that stem from the discretization of Ω. On expanding the trial and test functions as a linear combination of these basis functions and substituting them in (4), and using the arbitrariness of the test coefficients, we obtain the following linear system of equations:

$$\boldsymbol{K}\boldsymbol{d} = \boldsymbol{f}, \quad K_{ij} = a_h(\phi_i, \phi_j), \quad f_i = (g_N, \phi_i)_{\Gamma_N, h}, \tag{5}$$

where $\boldsymbol{d}$ is the unknown coefficient vector, $\boldsymbol{K}$ is the stiffness matrix, and $\boldsymbol{f}$ is the external force (load) vector.

We now introduce a few function space definitions, and prepare the reader by providing a roadmap of what lies ahead in this section. For a domain D, let $\mathbb{P}_k(D)$ denote the space of polynomials up to degree k on D. In this paper, we consider first-order virtual elements and require $\mathbb{P}_1(D)$, which is the space of linear polynomials on D. For each element E, we define the local

virtual element space $V^h(E)$ that includes the linear polynomials $\mathbb{P}_1(E) = \text{span}\{1, x, y\}$ as a subspace, and the global virtual element space V^h that is defined on Ω. Any virtual element function v^h in $V^h(E)$ is uniquely characterized by its vertex values, also dubbed the *degrees of freedom* (DOFs), which allows us to compute the elliptic projection $\Pi^\nabla v^h$ onto linear polynomials. For the X-VEM, we introduce the enriched local and global virtual element spaces, i.e., $V_X^h(E)$ and V_X^h, which incorporate some specific information at the element-level about the behavior of the weakly singular harmonic solution (denoted by ψ) or possibly a discontinuous solution. Accordingly, we define the more general projection operator $\Pi_X^\nabla v_X^h$ onto $\text{span}\{1, x, y, \psi\}$, which makes it possible to construct the extended virtual element bilinear form $a_h(\cdot, \cdot)$ used in (4). We also discuss why ψ being harmonic ($\Delta\psi = 0$) is crucial to guaranteeing that the projection $\Pi_X^\nabla v_X^h$ is computable from the degrees of freedom of v_X^h.

3.1. Mesh definition and regularity assumptions

Let $\mathcal{T} = \{\Omega_h\}_h$ be a family of decompositions of Ω into nonoverlapping polygonal elements E with nonintersecting boundary ∂E, barycenter $\boldsymbol{x}_E := (x_E, y_E)$, area $|E|$, and diameter $h_E = \sup_{\boldsymbol{x}, \boldsymbol{y} \in E} |\boldsymbol{x} - \boldsymbol{y}|$. The subindex h that labels each mesh Ω_h is the maximum of the diameters h_E of the elements of that mesh. The number of vertices of element E is denoted by N_E. The boundary of E is formed by straight edges, and the polygon E has N_E edges. The vertices of the polygonal element E are oriented in counter-clockwise order and their coordinates are denoted by $\boldsymbol{x}_k := (x_k, y_k)$, $k = 1, 2, \ldots, N_E$; for convenience, we also use $\boldsymbol{x}_k$ as a label for the k-th vertex. We denote the unit normal vector to edge $e \in \partial E$ by $\boldsymbol{n}_{E,e}$. Each vector $\boldsymbol{n}_{E,e}$ points out of E, and for ease of notation we let $\boldsymbol{n}_e := \boldsymbol{n}_{E,e}$.

The following mesh regularity assumptions are usually considered in the convergence analysis of the conforming VEM [9, 12]. Although the convergence analysis of the X-VEM is beyond the scope of this paper, we present such assumptions to characterize the geometry of the elements in the polygonal meshes, which is pertinent to our formulation.

Mesh regularity assumptions. There exists a positive constant ϱ independent of h (hence, also of Ω_h) such that for every polygonal element $E \in \Omega_h$ it holds that

(*i*) E is star-shaped with respect to a disk with radius $\geq \varrho h_E$; and

(*ii*) for every edge $e \in \partial E$ it holds that $h_e \geq \varrho h_E$.

Remark 3.1. *The restriction of E being star-shaped in* (*i*) *implies that all the elements are* simply connected *subsets of* $\mathbb{R}^2$. *The scaling assumption in* (*ii*) *implies that the number of edges on the boundary of any element is uniformly bounded over the whole mesh family* $\mathcal{T}$. *Weaker assumptions have been investigated by Beirão da Veiga et al.[21] and Brenner et al. [22], which confirm the robustness of the method on even more general meshes.*

3.2. Conforming virtual element space

On every polygonal element E with boundary ∂E, we define the standard local virtual element space

$$V^h(E) = \left\{ v^h \in H^1(E) \; : \; \Delta v^h = 0, \; v^h|_{\partial E} \in C^0(\partial E), \; v^h|_e \in \mathbb{P}_1(e) \; \forall e \in \partial E \right\}. \tag{6}$$

The space $V^h(E)$ contains all harmonic functions defined on E whose trace on the elemental boundary ∂E is a continuous piecewise-linear polynomial. A straightforward consequence of definition (6) is that the linear polynomials $\mathbb{P}_1(E) = \text{span}\{1, x, y\}$ (1, x, y are monomials on E), are a subspace of $V^h(E)$. However, in the implementation it is prudent to use the set of *scaled monomials* so that all functions are $O(1)$:

$$m_1(\boldsymbol{x}) = 1, \quad m_2(\boldsymbol{x}) = \frac{x - x_E}{h_E}, \quad m_3(\boldsymbol{x}) = \frac{y - y_E}{h_E}. \tag{7}$$

It is evident that $\mathbb{P}_1(E) = \text{span}\{m_1, m_2, m_3\}$, since the scaled monomials are also a basis of $\mathbb{P}_1(E)$.

Any virtual element function $v^h \in V^h(E)$ is uniquely determined by its vertex values, which are the degrees of freedom of v^h. In the FEM, it is common to associate *nodes* with the *vertices* of an element, and hence the two choices refer to the same entity in this paper. The proof of the unisolvence of the vertex values in $V^h(E)$ is given in [9]. Using only this information about v^h, we compute the *elliptic projection operator* $\Pi^\nabla : V^h(E) \to \mathbb{P}_1(E)$, which for $v^h \in V^h(E)$, is the solution of the variational problem [9]:

$$\int_E \nabla\Pi^\nabla v^h \cdot \nabla q \, d\boldsymbol{x} = \int_E \nabla v^h \cdot \nabla q \, d\boldsymbol{x} \quad \forall q \in \mathbb{P}_1(E), \tag{8}$$

with the additional condition

$$\int_{\partial E} (\Pi^\nabla v^h - v^h) \, ds = 0. \tag{9}$$

To prove the computability of $\Pi^\nabla v^h$ we reformulate (8) as a linear system. To this end, we expand the linear polynomial $\Pi^\nabla v^h$ on either $\{1, x, y\}$ or $\{m_1, m_2, m_3\}$ and substitute such an expansion on the left-hand side of (8). The coefficient matrix of the resulting linear system is the stiffness matrix computed on the monomial (or scaled monomial) basis; the unknowns are the coefficients of the expansion of $\Pi^\nabla v^h$; and the right-hand side is given by the integrals on the right of (8), for every q taken in the polynomial basis. These latter integrals are computable by using only the degrees of freedom of v^h and the fact that q is a known polynomial. Indeed, an integration by parts yields

$$\int_E \nabla\Pi^\nabla v^h \cdot \nabla q \, d\boldsymbol{x} = -\int_E v^h \Delta q \, d\boldsymbol{x} + \sum_{e \in \partial E} \int_e v^h \boldsymbol{n}_e \cdot \nabla q \, ds. \tag{10}$$

The volume term on the right vanishes because the Laplacian of a linear polynomial is zero; the edge integrals are computable because the degrees of freedom of v^h allow us to reconstruct the trace of v^h on each edge through linear interpolation. Finally, we note that the boundary integral in (9) is also computable after splitting it into edge subintegrals because the degrees of freedom of v^h allows us to interpolate the trace of v^h on the edge.

Remark 3.2. *The projection operator is polynomial preserving since $\Pi^\nabla q = q$ for $q \in \mathbb{P}_1(E)$. This property is fundamental to show that the standard virtual element method is linearly consistent, i.e., it satisfies the patch test on any linear solution.*

6

The global conforming virtual element space V^h (subordinate to the mesh Ω_h) is obtained by gluing together all the elemental spaces $V^h(E)$ to provide a conforming subspace of the functional space $H^1(\Omega)$. The formal definition reads as:

$$V^h := \left\{ v^h \in H^1(\Omega) \; : \; v^h|_E \in V^h(E) \;\; \forall E \in \Omega_h \right\}. \tag{11}$$

The degrees of freedom of the virtual element functions in V^h are given by collecting all the nodal values at the nodes of the mesh. The unisolvence of the degrees of freedom of V^h is an immediate consequence of the unisolvence of the degrees of freedom of each local virtual element space $V^h(E)$. The space V^h is conforming since the trace of any virtual element function on any inter-element edge only depends on the degrees of freedom of that function associated with that edge.

3.3. Extended virtual element space and the elliptic projection

To fix ideas, we first define the local virtual element space enriched with the harmonic function ψ on the polygonal element E as:

$$V_X^h(E) := V^h(E) + \psi V^h(E). \tag{12}$$

It follows from (12) that any enriched virtual element function is the sum of two terms, $v_X^h = v_0^h + \psi v_1^h$, where v_0^h and v_1^h are functions of the standard virtual element space $V^h(E)$. Consequently, the degrees of freedom that uniquely characterize the enriched virtual element function v_X^h are now given by two distinct sets of nodal values: $\{v_0^h(\boldsymbol{x}_k)\}_{k=1}^{N_E}$ and $\{\psi(\boldsymbol{x}_k)v_1^h(\boldsymbol{x}_k)\}_{k=1}^{N_E}$.

The enriched space $V_X^h(E)$ contains both the linear polynomials $\mathbb{P}_1(E)$ and functions of the form $\psi\mathbb{P}_1(E)$, namely, ψ, $x\psi$, and $y\psi$. Harmonic functions ψ, which are used as enrichment functions for the L-shaped domain problem in Section 5.3, are of the form (polar coordinates) $\psi(r,\theta) = r^\lambda f(\theta)$, where $0 < \lambda < 1$ is the strength of the singularity. To use a function ψ that is $O(1)$, we scale ψ by $\psi_0 = h^\lambda$. From the above considerations, it is natural to consider the two extended polynomial spaces defined below and denoted by $\mathbb{P}_{1,0}^X$ and $\mathbb{P}_{1,1}^X$ as possible candidates for the construction of an extended elliptic projection. However, we anticipate that only the first one can lead to a computable projector operator. This fact is expounded in Remark 3.3. Now, the following inclusion holds:

$$\mathbb{P}_{1,\ell}^X = \mathbb{P}_1(E) + \psi\mathbb{P}_\ell(E) \subset V_X^h(E) \quad \text{for } \ell = 0, \, 1, \tag{13a}$$

where

$$\mathbb{P}_{1,0}^X = \operatorname{span}\{1, \, x, \, y, \, \psi\} = \operatorname{span}\{m_1, \, m_2, \, m_3, \, \psi/\psi_0\}, \tag{13b}$$

and

$$\mathbb{P}_{1,1}^X = \operatorname{span}\{1, \, x, \, y, \, \psi, \, x\psi, \, y\psi\} = \operatorname{span}\{m_1, \, m_2, \, m_3, \, m_1\psi/\psi_0, \, m_2\psi/\psi_0, \, m_3\psi/\psi_0\}. \tag{13c}$$

We point out that the trace of an enriched virtual element function on an element edge $e \in \partial E$ may not be a linear polynomial due to the presence of ψ in the definition (12); i.e., in general, it lies in $\mathbb{P}_1(e) + \psi\mathbb{P}_1(e)$.

To build the enriched bilinear form a_h, we define the extended elliptic projection operator $\Pi^\nabla_X : V^h_X(E) \to \mathbb{P}^X_{1,0} = \text{span}(1, x, y, \psi)$ for each element E. For a given $v^h_X \in V^h_X(E)$, the extended elliptic projection $\Pi^\nabla_X v^h_X$ is the solution of the variational problem:

$$\int_E \nabla \Pi^\nabla_X v^h_X \cdot \nabla q_X \, d\boldsymbol{x} = \int_E \nabla v^h_X \cdot \nabla q_X \, d\boldsymbol{x} \quad \forall q_X \in \mathbb{P}^X_{1,0}(E), \tag{14}$$

with the additional condition

$$\int_{\partial E} (\Pi^\nabla_X v^h_X - v^h_X) \, ds = 0. \tag{15}$$

Similar to its counterpart in the standard virtual element space $V^h(E)$, the projection $\Pi^\nabla_X v^h_X$ onto the subspace $\mathbb{P}^X_{1,0}(E)$ is computable from the degrees of freedom of v^h_X. In fact, an integration by part yields:

$$\int_E \nabla \Pi^\nabla_X v^h_X \cdot \nabla q_X \, d\boldsymbol{x} = -\int_E v^h_X \Delta q_X \, d\boldsymbol{x} + \sum_{e \in \partial E} \int_e v^h_X \boldsymbol{n}_e \cdot \nabla q_X \, ds, \tag{16}$$

which must hold for any function $q_X \in \text{span}(1, x, y, \psi)$. On the right-hand side, the volume integral is zero because $\Delta q_X = 0$ for such q_X (recall that ψ is a harmonic function), and the edge integrals on ∂E are computable since $v^h_X = v^h_0 + \psi v^h_1$, and the trace of the standard virtual element functions v^h_0 and v^h_1 can be interpolated from their degrees of freedom. In general, the computation of $\Pi^\nabla_X v^h_X$ may involve the numerical integration of weakly singular functions, and therefore, special cubature schemes are required in order to achieve the required accuracy, see Section 5.1.

Remark 3.3. *It is worth noting that the extended elliptic projection operator that projects onto $\mathbb{P}_{1,1}(E)$, which is defined in (13), is noncomputable. In fact, although ψ is a harmonic function, the volume integral on the right-hand side of (16) would have nonharmonic integrands. For example, consider $q_X = x\psi$. In this case, on denoting $\boldsymbol{e}_1 = \nabla(x) = (1, 0)^T$, we obtain*

$$\Delta(x\psi) = \nabla \cdot \nabla(x\psi) = \nabla \cdot (x\nabla\psi + \psi\boldsymbol{e}_1) = x\Delta\psi + \nabla\psi \cdot \boldsymbol{e}_1 = \nabla\psi \cdot \boldsymbol{e}_1.$$

Therefore, on choosing $q_X = x\psi$ in (16), the volume integral

$$-\int_E v^h_X \nabla\psi \cdot \boldsymbol{e}_1 \, d\boldsymbol{x}$$

on the right-hand side remains, which is noncomputable from the degrees of freedom of v^h_X, as we do not have any information about the moments of v^h_X against the derivatives of ψ.

Remark 3.4. *The extended projection operator is still polynomial preserving since $\Pi^\nabla_X q_X = q_X$ for $q_X \in \text{span}\{1, x, y\}$, and $\Pi^\nabla_X \psi = \psi$ also holds. Therefore, we can write $\Pi^\nabla_X \mathbb{P}^X_{1,0}(E) = \mathbb{P}^X_{1,0}(E)$. Nonetheless, it is evident that $\Pi^\nabla_X q_X \neq q_X$ for $q_X \in \{x\psi, y\psi\}$, so even though the enriched space contains $x\psi$, $y\psi$ and ψ, as well as their linear combinations, the* patch test *using $x\psi$ and $y\psi$ as possible exact solutions would not be met. However, this is not an issue since $x\psi$ and $y\psi$ and their linear combinations are not harmonic functions, cf. Remark 3.3, and cannot be chosen as exact solutions of problem (2) for the patch test.*

Remark 3.5. *It should be pointed out that the approach described in this Section is applicable as long as the enrichment function ψ is regular enough on E (e.g., $\psi \in H^1(E)$), so that integration by parts in (16) can be carried out. For instance, this is the case of weakly singular enrichment functions, which are used in the L-shaped domain problem discussed in Section 5.3. On the contrary, a different strategy must be adopted for the case of an enrichment function ψ discontinuous over E, whose gradient is not computable on E. The reader is referred to Section 4.2 for further details on a viable approach to overcome this additional difficulty.*

3.4. Bilinear form and linear functional

At this point, the construction of the X-VEM is straightforward and follows the procedural steps outlined for the virtual element method [9]. We define the discrete bilinear form $a_h(u_X^h, v_X^h)$ for $u_X^h, v_X^h \in V_X^h$ as the sum of elemental contributions

$$a_h(u_X^h, v_X^h) = \sum_{E \in \Omega_h} a_h^E(u_X^h, v_X^h), \tag{17}$$

where each local bilinear form is given by

$$a_h^E(u_X^h, v_X^h) = \int_E \nabla \Pi_X^\nabla u_X^h \cdot \nabla \Pi_X^\nabla v_X^h \, d\boldsymbol{x} + S^E\big((I - \Pi_X^\nabla)u_X^h, (I - \Pi_X^\nabla)v_X^h\big). \tag{18}$$

In (18), $S^E(\cdot, \cdot)$ is *any* symmetric positive definite bilinear form for which there exist two positive constants c_* and c^*, independent of h and the shape of the element, such that

$$c_* a^E(v_X^h, v_X^h) \le S^E(v_X^h, v_X^h) \le c^* a^E(v_X^h, v_X^h) \quad \forall v_X^h \in V_X^h(E) \text{ with } \Pi_X^\nabla v_X^h = 0. \tag{19}$$

Here, $a^E(\cdot, \cdot)$ is the local coercive and continuous bilinear form:

$$a^E(u, v) = \int_E \nabla u \cdot \nabla v \quad \forall u, v \in H^1(E).$$

Effective choices for the stabilization terms are investigated in [23, 24]. By construction, the bilinear form $a_h^E(\cdot, \cdot)$ satisfies the following properties:

- *linear consistency*: for all $v_X^h \in V_X^h(E)$ and linear polynomials $q_X \in \mathbb{P}_1(E)$ it holds that

$$a_h^E(v_X^h, q_X) = a^E(v_X^h, q_X); \tag{20}$$

- *ψ-consistency*: for all $v_X^h \in V_X^h(E)$ it holds that

$$a_h^E(v_X^h, \psi) = a^E(v_X^h, \psi); \tag{21}$$

- *stability*: there exists two positive constants α_*, α^*, independent of h and E, such that

$$\alpha_* a^E(v_X^h, v_X^h) \le a_h^E(v_X^h, v_X^h) \le \alpha^* a^E(v_X^h, v_X^h) \quad \forall v_X^h \in V_X^h(E). \tag{22}$$

In particular, the first term in (18) ensures the linear and ψ-consistency of the method, i.e., the patch test, since $\Pi_X^\nabla q_X = q_X$ for $q_X \in \text{span}\{1, x, y, \psi\}$. The second term in (18) ensures that the X-VEM is stable—choose $\alpha_* = 1 + c_*$ and $\alpha^* = 1 + c^*$. In the next section, we build the extended elliptic projection operator and provide a suitable choice for the stabilization term $S^E(\cdot, \cdot)$.

We conclude this section with the formula for the right-hand side functional, which is given by

$$\left(g_N, v_X^h\right)_{\Gamma_N} = \sum_{e \in \Gamma_N} \int_e g_N v_X^h \, ds.$$

This functional is clearly computable because g_N is a known function and the trace of v_X^h on each edge $e \subset \Gamma_N$ is computable on interpolating the edge degrees of freedom.

4. Numerical implementation

4.1. Enrichment with a weakly singular function

As in the FEM, the functions of the global virtual element space V^h are continuous on Ω_h since the trace is conforming across the inter-element boundaries. Recall that N_E is the number of vertices (nodes) of element E. We can write any virtual element function of the local space $V^h(E)$ as the Lagrange interpolation of the N_E canonical basis functions denoted by φ_j for $j = 1, \ldots, N_E$, which are associated with the vertices (nodes) $\boldsymbol{x}_j$ of E. More precisely, the basis function φ_j takes on the value 1 at the j-th node $\boldsymbol{x}_j$, and zero at all the other nodes. The restriction of φ_j to E is zero as in the FEM if $\boldsymbol{x}_j$ does not belong to E; hence, φ_j has compact support, with the support region being over the 1-ring of elements that surround node $\boldsymbol{x}_j$. If E belongs to the support of φ_j, then the restriction of φ_j to E is in $V^h(E)$, which implies that the restriction of φ_j is a harmonic function on E and has a continuous piecewise linear trace on ∂E. Let the mesh Ω_h consist of N nodes. Then, it is readily seen that the set consisting of N basis functions φ_j defined in Ω_h forms a partition-of-unity (PU) on Ω_h:

$$\sum_{j=1}^{N} \varphi_j(\boldsymbol{x}) = 1 \quad \forall \boldsymbol{x} \in \Omega_h. \tag{23}$$

Likewise, the subset of basis functions that are associated with element E (known as *shape functions* of the element) form a PU in E.

We now provide a broader definition than that implied by (12). Any virtual element function of the extended space $V_X^h(E)$ can be written as:

$$v_X^h(\boldsymbol{x}) = \sum_{i \in \mathbb{I}} \varphi_i(\boldsymbol{x}) v_i^0 + \sum_{j \in \mathbb{J} \subseteq \mathbb{I}} \psi(\boldsymbol{x}) \varphi_j(\boldsymbol{x}) v_j^1 \quad \forall \boldsymbol{x} \in E, \tag{24}$$

where $\mathbb{I}$ refers to the index set consisting of the nodes of the element E, $\mathbb{J}$ is the subset of $\mathbb{I}$ indexing the enriched nodes and v_j^0 and v_j^1 are the nodal degrees of freedom of the standard virtual element functions v_0^h and v_1^h. It follows naturally that the set of functions $\{\phi_k\}_{k \in \mathbb{K}}$ defined on E and given by

$$\{\phi_k\}_{k=1}^{\text{card}(\mathbb{K})} = \{\varphi_i\}_{i \in \mathbb{I}} \cup \{\psi \varphi_j\}_{j \in \mathbb{J} \subseteq \mathbb{I}} \tag{25}$$

10

is a basis for the local enriched space $V_X^h(E)$. Clearly, $\text{card}(\mathbb{K}) = \text{card}(\mathbb{I}) + \text{card}(\mathbb{J})$. From (24), we observe that if $\mathbb{J} = \mathbb{I}$ (all nodes of E are enriched), then a PU exists on E and ψ resides in the local enriched virtual element space. However, if fewer than N_E nodes are enriched, then a PU does not exist on E and the function ψ is not contained in $V_X^h(E)$. For example, if only one node of E is enriched, say node 1, then we no longer have the extended space given in (12), but instead:

$$V_X^h(E) := V^h(E) + \text{span}\{\psi\varphi_1\}, \tag{26}$$

where φ_1 is the shape function associated with node 1.

To construct the local stiffness matrix from the extended projection operator Π_X^∇ that maps the enriched virtual function v_X^h onto linear monomials and ψ, we consider either *full* enrichment or *partial* enrichment on the element E. A partially enriched element, also referred to as a *blending element* in the extended finite element literature, is an element where only a subset of nodes of the element are enriched. The local stiffness matrix of a blending element E is built by considering all the standard virtual element shape functions associated with the nodes of E and only the enriched basis functions associated with the nodes of E that are enriched. Even if element E is only partially enriched, due to the presence of partitioned pieces of ψ through the enriched nodal shape functions, we should expect an improvement of the approximation property of the X-VEM vis-à-vis the standard VEM. To realize this end, we adopt the Π_X^∇ projection operator, which ensures that the consistent stiffness matrix so formed (and hence K_E) can exactly reproduce ψ at the nodes and its use leads to improvements in accuracy. The results in Section 5.3.1 when only a single node in the mesh is enriched for the L-shaped domain Laplace problem bears this out.

4.1.1. Matrix representation of the elliptic projector Π_X^∇

Assuming *full* enrichment and using the set of Lagrange basis functions introduced in the previous section, we represent the projection operator Π_X^∇ defined on E as a $4 \times 2N_E$ matrix $\mathbf{\Pi}^X$. The j-th column of $\mathbf{\Pi}^X$ contains the coefficients of $\Pi_X^\nabla \phi_j$, the projection of the j-th basis function ϕ_j, on the scaled monomials augmented with ψ/ψ_0, i.e., on $\{m_1, m_2, m_3, \psi/\psi_0\}$. In other words, denote the j-th column of $\mathbf{\Pi}^X$ by $(\boldsymbol{a}_j^X)^T = \{a_{1j}^X, a_{2j}^X, a_{3j}^X, a_{4j}^X\}^T$. Then, the projection of ϕ_j onto $\{m_1, m_2, m_3, \psi/\psi_0\}$ is given by

$$\Pi_X^\nabla \phi_j(\boldsymbol{x}) = a_{1j}^X m_1(\boldsymbol{x}) + a_{2j}^X m_2(\boldsymbol{x}) + a_{3j}^X m_3(\boldsymbol{x}) + a_{4j}^X \frac{\psi(\boldsymbol{x})}{\psi_0}.$$

Let m_i^X for $i = 1, \ldots, 4$ denote the scaled functions that form a basis for the extended space $\mathbb{P}_{1,0}^X = \mathbb{P}_1(E) + \psi\mathbb{P}_0(E)$. Here, m_i^X for $i = 1, 2, 3$ are the scaled monomials and $m_4^X = \psi/\psi_0$ is the scaled enriched function. We compute matrix $\mathbf{\Pi}^X$ by solving the linear system

$$\boldsymbol{G}^X \mathbf{\Pi}^X = \boldsymbol{B}^X, \tag{27}$$

where $\boldsymbol{G}^X = (G_{ij}^X)$ is given by

$$G_{ij}^X = \begin{cases} \dfrac{1}{N_E} \displaystyle\sum_{k=1}^{N_E} m_j^X(\boldsymbol{x}_k) & \text{for } i = 1, \ j = 1, \ldots, 4 \\[4mm] \displaystyle\int_E \nabla m_i^X(\boldsymbol{x}) \cdot \nabla m_j^X(\boldsymbol{x}) \, d\boldsymbol{x} & \text{for } i > 1, \ j = 1, \ldots, 4 \end{cases}, \tag{28}$$

11

and $\boldsymbol{B}^X = (B_{ij}^X)$ is given by

$$
B_{ij}^X = \begin{cases} \dfrac{1}{N_E} \sum_{k=1}^{N_E} \phi_j(\boldsymbol{x}_k) & \text{for } i = 1, \ j = 1, \ldots, 2N_E, \\[4mm] \displaystyle\int_E \nabla m_i^X(\boldsymbol{x}) \cdot \nabla \phi_j(\boldsymbol{x}) \, d\boldsymbol{x} & \text{for } i > 1, \ j = 1, \ldots, 2N_E \end{cases} \tag{29}
$$

In addition, the degrees-of-freedom matrix, $\boldsymbol{D}^X$, is defined as:

$$
\boldsymbol{D}^X = \begin{bmatrix} \mathbf{dof}(m_1^X) & \mathbf{dof}(m_2^X) & \mathbf{dof}(m_3^X) & \mathbf{0} \\ \mathbf{0} & \mathbf{0} & \mathbf{0} & \mathbf{dof}(m_1^X) \end{bmatrix}, \tag{30}
$$

where $\mathbf{dof}(m_i^X)$ is the column vector collecting the degrees of freedom of m_i^X.

Integrals in (28) are computable, since integrands are known over the element E. Moreover, integrals in (29) are also computable since they can be reduced to the element boundary ∂E using (16). In particular, the matrix entries G_{ij}^X ($i, j = 1, 2, 3$) and B_{ij}^X ($i = 1, 2, 3, \ j = 1, \ldots, N_E$) are easily computed as the corresponding integrals of the standard VEM [13]. For example, on using the properties of the Lagrange basis functions ϕ_j, we have

$$
\frac{1}{N_E} \sum_{k=1}^{N_E} \phi_j(\boldsymbol{x}_k) = \frac{1}{N_E} \sum_{k=1}^{N_E} \delta_{jk} = \frac{1}{N_E}.
$$

However, distinct from standard VEM, the numerical computation of matrix entries G_{ij}^X and B_{ij}^X involving weakly singular integrands, such as G_{ij}^X ($i = 4, \ j = 1, \ldots, 4$) and B_{ij}^X ($i = 4, \ j = 1, \ldots, 2N_E$), requires special care in the choice of the cubature scheme to obtain a satisfactory level of accuracy. The effect of the numerical integration on the accuracy of the method is investigated in Section 5.1.

We have defined $\boldsymbol{B}^X$, $\boldsymbol{G}^X$, and $\boldsymbol{D}^X$ as the enriched counterparts of matrices $\boldsymbol{B}$, $\boldsymbol{G}$ and $\boldsymbol{D}$ that are used in the standard VEM, for which the relation $\boldsymbol{BD} = \boldsymbol{G}$ holds [13]. Analogously, it is readily shown that the equality $\boldsymbol{B}^X \boldsymbol{D}^X = \boldsymbol{G}^X$ is also met for the extended matrices.

4.1.2. Enriched stiffness matrix

On using (18), the stiffness matrix $\boldsymbol{K}_E := (K_{ij}^E)$ of the X-VEM is given by

$$
K_{ij}^E = (K_c^E)_{ij} + (K_s^E)_{ij} = \int_E \nabla \Pi_X^\nabla \phi_i \cdot \nabla \Pi_X^\nabla \phi_j \, d\boldsymbol{x} + S^E\big((I - \Pi_X^\nabla)\phi_i, (I - \Pi_X^\nabla)\phi_j\big), \tag{31}
$$

where the stabilizing function S^E is defined as [24]:

$$
S^E(v_h, w_h) = \alpha \, \text{trace}(\boldsymbol{K}_c^E) \sum_{\ell=1}^{N_E} \text{dof}_\ell(v_h) \, \text{dof}_\ell(w_h), \tag{32}
$$

where α is a scalar stabilization parameter and $\text{dof}_\ell(\cdot)$ is the functional that returns the value of the ℓ-th degree of freedom when applied to a virtual element function. We note here that multiplying the summation in (32) by the trace of $\boldsymbol{K}_c^E$ ensures that the stabilization term scales

like the consistency term. This is a standard approach within the VEM [25]. It is straightforward to prove that $a_h(\phi_i, \phi_j)$ satisfies the linear and ψ-consistency and the stability condition of Section 3.4, and that the stabilization term (32) satisfies the stability bounds (19). Now, let $\widehat{G}$ be the matrix obtained by setting the first row of G^X to zero and I the $2N_E \times 2N_E$ identity matrix. Then, we can reformulate (31) in matrix form:

$$K^E = K_c^E + K_s^E = (\mathbf{\Pi}_X^\nabla)^T \widehat{G} (\mathbf{\Pi}_X^\nabla) + \alpha \operatorname{trace}(K_c^E)(I - D^X\mathbf{\Pi}_X^\nabla)^T(I - D^X\mathbf{\Pi}_X^\nabla). \tag{33}$$

A different type of stabilization, with respect to (32), is the so-called diagonal stabilization, or *D-recipe*, defined in matrix form as follows:

$$K_s^E = (I - \mathbf{\Pi}_X^\nabla)^T S_d^E (I - \mathbf{\Pi}_X^\nabla), \tag{34}$$

where S_d^E is a diagonal matrix whose entries are given by [24, 26]:

$$(S_d^E)_{i,i} = \max\left(1, (K_c^E)_{i,i}\right). \tag{35}$$

Finally, alongside (35), we also propose the following alternative choice for the diagonal matrix S_d^E to be used in (34):

$$(S_d^E)_{i,i} = \max\left(\operatorname{trace}(K_c^E)/\operatorname{size}(K_c^E), (K_c^E)_{i,i}\right), \tag{36}$$

where $\operatorname{size}(K_c^E)$ represents the dimension of K_c^E. We will refer to this choice for the stabilization as the *modified D-recipe*.

4.2. Enrichment with a discontinuous function

Consider a crack γ that intersects some of the elements in a mesh, and define $d(\boldsymbol{x})$ as the signed distance from a point $\boldsymbol{x}$ to γ. For modeling strong discontinuities like a crack, it is convenient to consider enrichment with the generalized Heaviside function $H(\boldsymbol{x})$, which is equal to $+1$ for points with $d(\boldsymbol{x}) \geq 0$ ($\boldsymbol{x}$ is on or above the crack) and is -1 for points with $d(\boldsymbol{x}) < 0$ ($\boldsymbol{x}$ is below the crack).

As in the X-FEM, we enrich with $H(\boldsymbol{x})$ those nodes whose basis function support intersects the interior (tips of the crack not included) of the crack. In an element E that is cut by γ, we take $\mathbb{J} = \mathbb{I}$ and the extended virtual element approximation is:

$$v_X^h(\boldsymbol{x}) = \sum_{i \in \mathbb{I}} \varphi_i(\boldsymbol{x})v_i^0 + \sum_{j \in \mathbb{I}} H(\boldsymbol{x})\varphi_j(\boldsymbol{x})v_j^1 \quad \forall \boldsymbol{x} \in E. \tag{37}$$

We note that (37) suggests an extended virtual element space that is formally similar to (24). However, in contrast to the harmonic enrichment function ψ for weak singularities used in (24), the generalized Heaviside function $H(\boldsymbol{x})$ is not a solution of the variational problem (2). Furthermore, since the enriched virtual basis functions $\phi_j = H\varphi_j$ are not known along the crack, it can be easily shown that neither the standard VEM projection Π^∇ onto $\mathbb{P}_1(E)$ nor the extended projection Π_X^∇ onto $\mathbb{P}_{1,0}^X(E)$ are directly computable from the degrees of freedom of the method.

To deliver a viable solution, let the element E be partitioned by the discontinuity γ into two subdomains E^- and E^+. To represent two independent linear polynomials on E^- and E^+, we adopt the approach of Hansbo and Hansbo [18] and tailor it to the X-VEM. To this end, each

standard virtual shape function φ_j on E is written as the sum of two new virtual shape functions φ_j^- and φ_j^+ that are both discontinuous across the crack, and are defined as follows:

$$\varphi_j^+ = \begin{cases} 0 & \text{in } E^- \\ \varphi_j & \text{in } E^+ \end{cases}, \quad \varphi_j^- = \begin{cases} \varphi_j & \text{in } E^- \\ 0 & \text{in } E^+ \end{cases}. \tag{38}$$

Clearly, φ_j^- and φ_j^+ are harmonic and continuous functions in E^- and E^+, respectively, and $\varphi_j = \varphi_j^- + \varphi_j^+$. Proceeding likewise for all the nodes in the element, we can generate $2N_E$ discontinuous virtual basis functions, starting from the standard N_E virtual basis functions. Furthermore, as we will detail later on, we do so by doubling the nodal DOFs on the standard element. Therefore, the number of degrees of freedom for the element with an internal discontinuity is twice that of the original element, and a virtual element basis is constructed by considering two copies of the original virtual basis functions, restricted to E^- and E^+ respectively, as defined in (38). Therefore, formally we seek a discrete solution in the space $V_-^h(E) \cup V_+^h(E)$, where

$$V_-^h(E) = \left\{ v^h \in H^1(E^-) \; : \; \Delta v^h|_{E^-} = 0, \; v^h|_{\partial E^-} \in C^0(\partial E^-), \; v^h|_e \in \mathbb{P}_1(e) \; \forall e \in (\partial E \cap \partial E^-) \right\},$$

$$V_+^h(E) = \left\{ v^h \in H^1(E^+) \; : \; \Delta v^h|_{E^+} = 0, \; v^h|_{\partial E^+} \in C^0(\partial E^+), \; v^h|_e \in \mathbb{P}_1(e) \; \forall e \in (\partial E \cap \partial E^+) \right\}.$$

Space $V_-^h(E) \cup V_+^h(E)$ is not a subspace of $H^1(E)$ as we do not assume any regularity of the virtual element functions across the crack, so that a discontinuity is admissible. As we detail later on, virtual functions along interface edges are reconstructed by a suitable approximation.

On substituting (38) in (37), we obtain the following representation for the virtual element approximation on an element E that is cut by γ:

$$v_X^h(x) = \sum_{i \in \mathbb{I}} \left[\varphi_i^-(x) v_i^- + \varphi_i^+(x) v_i^+ \right] \quad \forall x \in E, \tag{39}$$

where v_i^- and v_i^+ are degrees of freedom associated with φ_i^- and φ_i^+, respectively. It is readily verified that

$$v_i^- = v_i^0 - v_i^1, \quad v_i^+ = v_i^0 + v_i^1, \tag{40}$$

which indicates that the virtual element approximations in (37) and (39) are equivalent. This correspondence has earlier been established for the representation of discontinuous fields on finite element meshes, see for example [19] and [27].

For virtual elements, the approximation form in (39) is preferable to the one in (37), since it provides a pathway to construct two independent linear polynomials on either side of γ. This leads to the satisfaction of the discontinuous patch test (see Section 5), whereas use of (37) as introduced earlier in Benvenuti et al. [28] does not.

In order to provide a feasible solution via use of (39), it is necessary to know the trace of the virtual shape functions φ_j along the crack, so that two separate projection operators $\Pi^{\nabla,-}$ onto $\mathbb{P}_1(E^-)$ and $\Pi^{\nabla,+}$ onto $\mathbb{P}_1(E^+)$ can be computed starting from the $2N_E$ nodal degrees of freedom. To this end, a convenient approximation for the trace of the j-th virtual shape function

φ_j along the crack is provided by a suitable approximating function $N_j(x)$ that is harmonic on the cracked element E. Such a function is built as a first-order polyharmonic spline [29]:

$$N_j(x) = \sum_{i=1}^{n} w_i \Psi(\|x - c_i\|) + a \cdot m(x), \tag{41}$$

where $w := \{w_1 \ldots w_n\}$ and $a := \{a_0 \ a_1 \ a_2\}$ are unknown, and $m(x) = \{1 \ x \ y\}$ is a linear basis. The first term in the above equation is a linear combination of n radial basis functions $\Psi(\cdot)$ centered at c_i, and the second term is a linear polynomial in x. Finally, w_i is a set of n weights, which has to be determined, together with the coefficients a_i ($i = 0, 1, 2$). We choose the function $\Psi(r) = \ln r$, which is the fundamental solution of the radial Laplace equation. With this choice, the function N_j is harmonic in the whole domain except where $x = c_i$. In order to avoid such singularities within the element, the n kernel points c_i are chosen by sampling n points $s_i \in \partial E$ and then moving the sampled points s_i in the outward normal direction n by a small fraction η of the element size, so that

$$c_i = s_i + \eta h_E n(s_i). \tag{42}$$

On each edge of the element, 8 sampling points are chosen with $\eta = 1/20$. The unknown vectors w and a are determined by minimizing an L^2 error norm on ∂E, which is approximated as a discrete sum of m collocation points p_i on the boundary of E, as follows:

$$\min_{w,a} \frac{1}{m} \sum_{i=1}^{m} [N_j(p_i) - b_j(p_i)]^2, \tag{43}$$

where $b_j(x)$ is the (known) trace of φ_j on the element boundary. The number of collocation points is chosen as $m = 3n$. The minimization of the discretized L^2 error in (43) leads to an overdetermined linear least squares system for the coefficient vectors w and a:

$$\begin{bmatrix} A & B^T \end{bmatrix} \begin{Bmatrix} w \\ a \end{Bmatrix} = b, \tag{44a}$$

where

$$A_{ij} = \Psi(\|p_i - c_j\|), \quad B = \begin{bmatrix} 1 & 1 & \cdots & 1 \\ p_1 & p_2 & \cdots & p_m \end{bmatrix}, \quad b = \left\{ b_j(p_1), \ b_j(p_2) \ldots \ b_j(p_m) \right\}^T. \tag{44b}$$

If the trace of φ_j along the crack is approximated by the trace of N_j (see Figs. 1a and 1b for examples of N_j computed along the crack in a hexagonal element), it is indeed possible to construct the two separate projection operators $\Pi^{\nabla,-}$ onto $\mathbb{P}_1(E^-)$ and $\Pi^{\nabla,+}$ onto $\mathbb{P}_1(E^+)$ starting from the $2N_E$ nodal degrees of freedom, as in the standard VEM.

We can now write the bilinear form as

$$a(\varphi_i, \varphi_j) = \int_E \nabla\varphi_i \cdot \nabla\varphi_j \, dx = \int_{E^-} \nabla\varphi_i^- \cdot \nabla\varphi_j^- \, dx + \int_{E^+} \nabla\varphi_i^+ \cdot \nabla\varphi_j^+ \, dx, \tag{45}$$

15
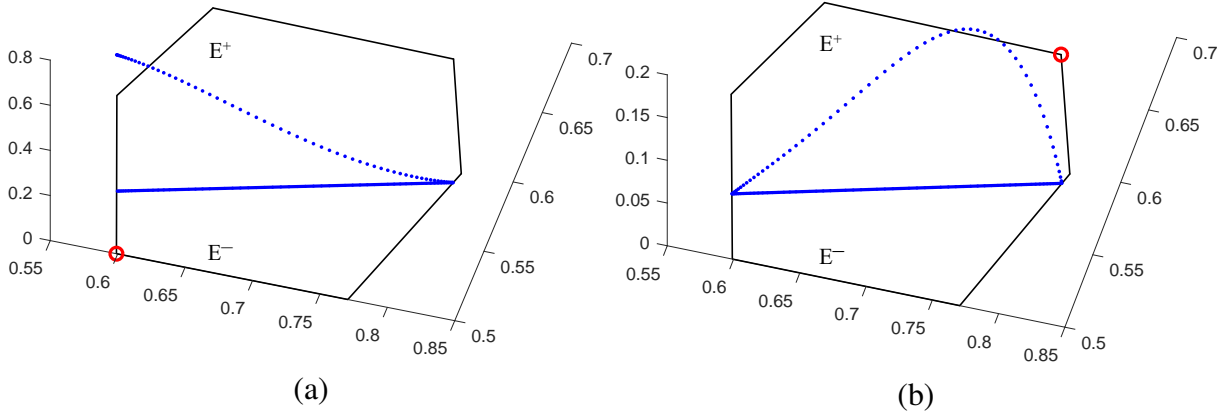
Figure 1: Trace of the approximation N_j of φ_j along the crack on a hexagonal element, where φ_j is the virtual shape function associated with the node j that is marked by the circle in (a) and (b).

which is the sum of a consistency term plus a stabilization term. The entries of the consistent part of the local stiffness matrix are

$$(K_c^E)_{i^- j^-} = \int_{E^-} \nabla \Pi^{\nabla,-} \varphi_i^- \cdot \nabla \Pi^{\nabla,-} \varphi_j^- \, d\boldsymbol{x}, \tag{46a}$$

$$(K_c^E)_{i^+ j^+} = \int_{E^+} \nabla \Pi^{\nabla,+} \varphi_i^+ \cdot \nabla \Pi^{\nabla,+} \varphi_j^+ \, d\boldsymbol{x}, \tag{46b}$$

$$(K_c^E)_{i^+ j^-} = K_{i^- j^+}^c = 0, \tag{46c}$$

where we adopt the subscripts i^-, i^+ to denote the two degrees of freedom associated with the virtual basis functions φ_i^- and φ_i^+, respectively. On the other hand, the matrix entries of the stabilization term are

$$(K_s^E)_{i^- j^-} = S^E((I - \Pi^{\nabla,-})\varphi_i^-, (I - \Pi^{\nabla,-})\varphi_j^-), \tag{47a}$$

$$(K_s^E)_{i^+ j^+} = S^E((I - \Pi^{\nabla,+})\varphi_i^+, (I - \Pi^{\nabla,+})\varphi_j^+), \tag{47b}$$

$$(K_s^E)_{i^+ j^-} = (K_s^E)_{i^- j^+} = 0, \tag{47c}$$

where possible choices for $S^E(\cdot, \cdot)$ have been previously defined in Section 4.1.2. On a unit square element, Fig. 2 illustrates the difference between the standard virtual element projection onto $\mathbb{P}_1(E)$ of one of the four virtual basis functions and the separate projections onto $\mathbb{P}_1(E^-)$ and $\mathbb{P}_1(E^+)$ of the two corresponding basis functions in the proposed X-VEM.

5. Numerical results

In this section, we first show how the presence of a radial singularity renders the choice of numerical cubature to be crucial to obtain accurate results (Section 5.1). Then, results of the extended patch tests are presented in Section 5.2. Finally, in Section 5.3 and Section 5.4, we describe the extended virtual element solutions for problems with singular and discontinuous primal fields.

16
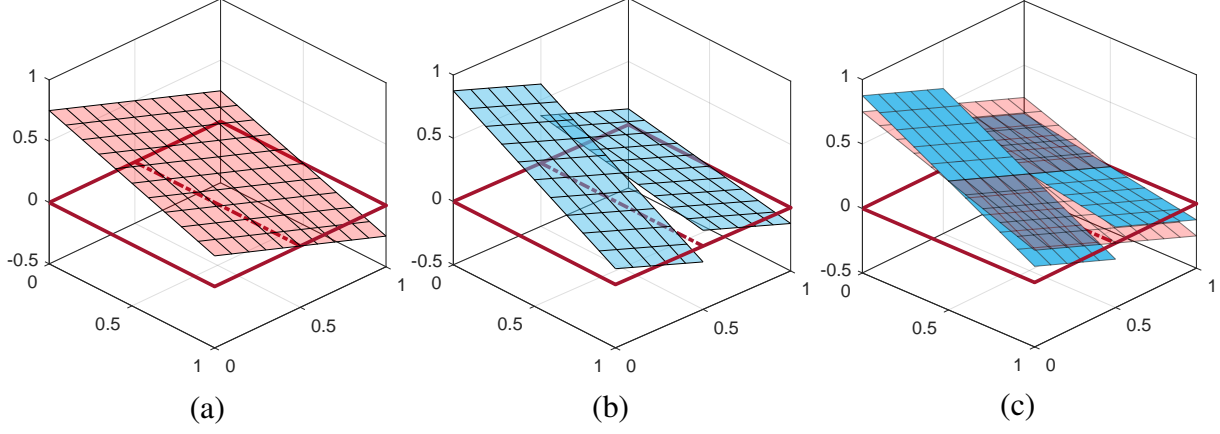
Figure 2: (a) Projection onto $\mathbb{P}_1(E)$ of one of the virtual basis functions φ_j of a square element. (b) Separate projections of φ_j^+ and φ_j^- onto $\mathbb{P}_1(E^+)$ and $\mathbb{P}_1(E^-)$, respectively. (c) Superposition of the three projections.

5.1. Numerical integration

Consider the enrichment function $\psi(r) = r^\lambda$, where $r = \sqrt{x^2 + y^2}$ and $0 < \lambda < 1$. Let us examine a typical enriched stiffness matrix contribution that arises in the X-VEM. For a unit square element, consider the evaluation of the integral

$$\mathcal{I}_\lambda = \int_0^1 \int_0^1 \nabla\psi \cdot \nabla\psi \, d\boldsymbol{x} = \lambda^2 \int_0^1 \int_0^1 r^{2(\lambda-1)} \, d\boldsymbol{x}. \tag{48}$$

In light of the Laplace problem that follows in the next section, we select $\lambda = 1/3$. The exact result is: $\mathcal{I}_{1/3} = 0.2823793355343268$. The use of two cubature procedures, one general and one especially conceived for singular functions, has been investigated for the computations of integrals. The general procedure is a product Gauss cubature scheme for polygons proposed by Sommariva and Vianello in [30], also distributed as an open source `MATLAB` routine under the name `polygauss.m`. The enhanced procedure is based on the numerical integration of homogeneous functions on convex and nonconvex polygons and polyhedra, developed by Chin et al. [7], hereafter referred to by the acronym HNI. The `polygauss` approach relies on a Gauss-like cubature formula over convex, nonconvex and multiply connected polygons. The formula is exact for polynomials of degree at most $2n - 1$ using mn^2 nodes, where m is the number of sides that are not orthogonal to a given line, nor lying on it. This cubature scheme does not require triangulation of the domain, but relies directly on univariate Gauss-Legendre quadrature via Green's integral formula.

The HNI scheme allows to reduce integration of homogeneous functions over arbitrary convex and nonconvex polytopes to integration over the boundary facets of the polytope. By definition, a positively homogeneous function of degree q satisfies

$$f(\lambda\boldsymbol{x}) = \lambda^q f(\boldsymbol{x}) \tag{49}$$

for all $\boldsymbol{x}$ and where $\lambda > 0$. Given a two-dimensional domain M, bounded by ∂M, let $\boldsymbol{n}$ be the unit outward vector normal to ∂M and $d\sigma$ the differential length of the parametrized curve σ on ∂M. Then, given a homogeneous function f of degree q, applying Euler's homogeneous

function theorem and Stokes' theorem, it can be shown that

$$\int_M f(\boldsymbol{x})\, d\boldsymbol{x} = \frac{1}{2+q} \int_{\partial M} (\boldsymbol{x} \cdot \boldsymbol{n}) f(\boldsymbol{x})\, d\sigma. \tag{50}$$

If M is a polygonal domain with edges e_i ($i = 1, \ldots, m$), let $\boldsymbol{a}_i \cdot \boldsymbol{x} = b_i$ the line containing edge e_i, where the sign of b_i is determined such that $\boldsymbol{a}_i/\|\boldsymbol{a}_i\|$ is the outward normal to the polygon. Then, (50) reduces to

$$\int_M f(\boldsymbol{x})\, d\boldsymbol{x} = \frac{1}{2+q} \sum_{i=1}^{m} \frac{b_i}{\|\boldsymbol{a}_i\|} \int_{e_i} f(\boldsymbol{x})\, d\sigma. \tag{51}$$

On applying an nq-th point Gauss quadrature rule, (51) becomes

$$\int_M f(\boldsymbol{x})\, d\boldsymbol{x} = \frac{1}{2+q} \sum_{i=1}^{m} \frac{b_i}{\|\boldsymbol{a}_i\|} \sum_{j=1}^{nq} w_{ij} f(\boldsymbol{x}_{ij}). \tag{52}$$

With Gauss quadrature applied to the bounding line segments, (52) provides numerical integration with polynomial precision over arbitrary polygons. Such a scheme is particularly efficient when integrating a weakly singular homogeneous function over a two-dimensional domain, such as that encountered when numerically solving the Laplace problem on an L-shaped domain using the X-VEM. It is also pertinent in the computation of the matrix G defined in (28), stiffness matrix entries K_{ij}^E defined in (33), and strain energy computations as well. Indeed, if the singular point is within the domain of integration, then this leaves only the computation of an integral of a smooth function over the boundary of the polygon. Furthermore, if the singular point lies on the boundary and coincides with one of the bounding line segments, then no contribution arises from this line integral. If a weakly singular homogeneous function is singular at the origin and the i-th line segment passes through the origin, then we have $b_i/\|\boldsymbol{a}_i\| = 0$. These two observations reveal why the HNI scheme is effective for weakly singular functions. However, bounding line segments may still be very close to the singular point, resulting in a nearly singular integral. Polynomial approximation of such an integral is poor and requires many cubature points to attain sufficient accuracy. To optimize the distribution of integration points required on each line segment, we adopt an adaptive integration scheme that provides an optimized, custom cubature rule for each element. This allows such integrals to be calculated to a user-specified precision through an a posteriori estimation of the error (see [8] for further details).

The relative errors obtained with both `polygauss` and the adaptive HNI scheme [7, 8] are listed in Table 1. The advantages of the adaptive HNI method are striking and its use ensures sound accuracy and robustness, which is especially needed with enriched approximation spaces that can deliver high-accuracy.

5.2. Extended patch tests

As a verification of the X-VEM and a check for the proposed implementation, we perform a series of *extended patch tests* by using manufactured solutions for the Laplace equation $\Delta u = 0$ with Dirichlet boundary conditions on a L-shaped domain (see also Section 5.3), in order to ensure that the enrichment function can be exactly reproduced using the X-VEM. To this end,

Table 1: Relative error when $\mathcal{I}_{1/3}$ is computed with the adaptive HNI scheme [7, 8] and product Gauss cubature [30]. n_Q is the number of integration points; for the HNI method, n_Q integration points are used on the element boundary.

HNI		Gauss	
n_Q	Relative error	n_Q	Relative error
10	1.2×10^{-8}	8450	4.1×10^{-3}
20	3.9×10^{-11}	33282	1.7×10^{-3}
30	8.8×10^{-12}	132098	6.7×10^{-4}
40	2.0×10^{-16}	526338	2.7×10^{-4}

Table 2: Errors in the H^1 seminorm for the extended patch test on the L-shaped domain. For product Gauss cubature scheme, 8450 integration points within the element are used, whereas 40 integration points on the element boundary are used with the adaptive HNI scheme.

Exact solution	$\|u - u^h\|_{H^1}$	
ψ	HNI	Gauss
$r^{2/3} \sin(2\theta/3)$	7.4×10^{-9}	1.6×10^{-5}
$r^{1/2} \sin(\theta/2)$	2.9×10^{-8}	2.8×10^{-4}
$r^{1/3} \sin(\theta/3)$	1.3×10^{-7}	4.6×10^{-3}

we choose harmonic solutions ψ in polar coordinates (r, θ), centered on the domain re-entrant corner, that have a weak singularity in $r = 0$. Then, we appropriately set $g_D = \psi$ on the boundary $\Gamma = \Gamma_D$ ($\Gamma_N = \emptyset$). We use ψ as the enrichment function in the X-VEM.

We consider coarse meshes of square elements (12 elements) where all nodes in a mesh are enriched. The exact solutions ψ considered contain the radial term r^λ with $\lambda = \frac{2}{3}, \frac{1}{2}, \frac{1}{3}$. Table 2 shows the outcome of the extended patch tests for each reference solution employed, in terms of absolute errors in the H^1 seminorm. For the sake of comparison, integrals involved in these tests are computed by means of both a high-order product Gauss cubature rule (8450 evaluation points on each element) and the adaptive HNI method [7, 8]. For homogeneous polynomials, the latter approach allows to further reduce the integration to function evaluations at the edges of each polygonal element. This also avoids the evaluation of the enrichment function ψ at the location of the vertex singularity.

For all values of λ, Table 2 reveals that the adaptive HNI scheme delivers much better accuracy with far fewer points than product Gauss cubature, which points to the efficiency of the adaptive HNI method.

5.3. L-shaped domain with corner singularity

A well-known benchmark problem with a geometric corner singularity is the Laplace problem on an L-shaped domain. The boundary-value problem is posed as:

$$\Delta u = 0 \quad \text{in } \Omega, \tag{53a}$$

$$u = 0 \quad \text{on } \Gamma_D, \tag{53b}$$

$$\boldsymbol{n} \cdot \nabla u = g_N \quad \text{on } \Gamma_N, \tag{53c}$$

where Ω is shown in Fig. 3. Polar coordinates are used with the origin centered on the re-entrant corner. Following Strouboulis et al. [31], we choose the Neumann boundary data g_N

that is consistent with the exact solution [32]:

$$u(r, \theta) = r^{\frac{1}{3}} \sin \frac{\theta}{3}, \quad \nabla u(r, \theta) = \frac{r^{-2/3}}{3} \left[-\sin \frac{2\theta}{3} \boldsymbol{e}_1 + \cos \frac{2\theta}{3} \boldsymbol{e}_2 \right], \quad (54)$$

which has a derivative singularity at $r = 0$.
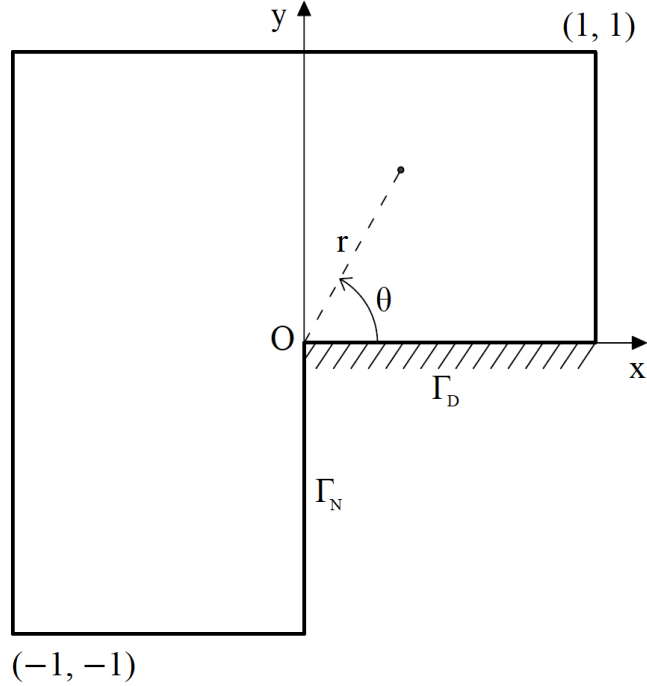
Figure 3: Geometry and boundary conditions for the L-shaped domain Laplace problem.

To compute matrix $\boldsymbol{K}_E$, we implement the elliptic projector described in Section 4.1.1. We adopt the stabilization (32), where the stabilization parameter α is set to 1. Diagonal stabilizations (see Section 4.1.2) are also investigated in the study. In the analyses, meshes consisting of squares, distorted quadrilaterals and general polygons are considered; polygonal meshes have been generated from Voronoi diagrams [33]. Two representative meshes are shown in Fig. 4.

5.3.1. Topological enrichment

We first study the case shown in Fig. 5 where only the node located at the vertex singularity is enriched. We refer to this strategy as *topological enrichment*. The expected convergence rate in strain energy for this case is $\min(2\lambda, 2p)$ [32], where λ is the order of the singularity at the corner and p is the degree of the polynomial approximating field. Since, for the problem at hand, $\lambda = 1/3$ and $p = 1$, we expect a convergence rate of $2\lambda = 2/3$. This sub-optimal convergence was also noted in previous finite element studies where enrichment for crack problems ($\lambda = 1/2$) is used [34].

A convergence study for the X-VEM is conducted by computing both the relative error in strain energy and the relative error in L^2 norm on a sequence of refined meshes. The relative error in strain energy is computed using

$$E = \frac{|a(\tilde{u}^h, \tilde{u}^h) - a(u, u)|}{a(u, u)}, \quad (55)$$

20
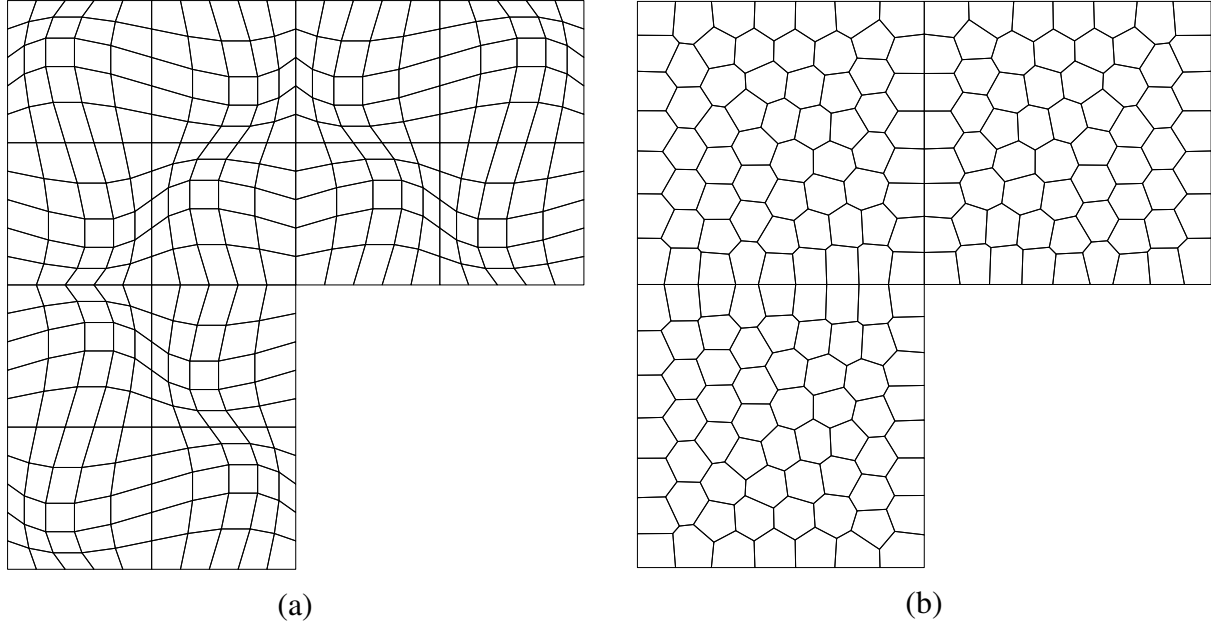
Figure 4: Representative meshes made of (a) distorted quadrilaterals and (b) convex polygons for the *L*-shaped domain problem.

where $a(u, u)/2 = 0.423569003301483$ is the exact strain energy and $\tilde{u}^h$ is the projection of the discrete solution u^h, defined as:

$$\tilde{u}^h = \sum_{K \in \mathcal{T}} \Pi_K^\nabla u^h,$$

with $\Pi_K^\nabla = \Pi^\nabla$ for non-enriched elements and $\Pi_K^\nabla = \Pi_X^\nabla$ for elements containing enriched nodes. The reason for this choice is that it is not possible to compute the *true* energy associated with u^h, since the virtual functions are not explicitly known [35].

Figs. 6 and 7 show the convergence plots of the relative error in strain energy and the relative L^2 error, respectively. The expected convergence rate (denoted by R) is indicated in the plots. All methods converge in both strain energy and in the L^2 norm with a rate close to 2/3, which is in agreement with theory. The results from the X-VEM are relatively insensitive to the type of mesh (quadrilaterals or polygons); however they are consistently much more accurate than the results obtained using the standard VEM. The sensitivity of the errors in strain energy to the choice of the stabilization parameter α on quadrilateral meshes is presented in Fig. 8. The choice $\alpha = 1$ yield results that are proximal to the X-FEM, whereas values of α smaller than 1 deliver considerably better accuracy than the X-FEM. Moreover, Fig. 8 also contains results for the diagonal stabilization, both in the standard form (35) and in the modified form (36). Notably, the *modified D-recipe* allows for improved accuracy over the other stabilizations, with the advantage of not requiring any tunable parameters.

5.3.2. Geometric enrichment

It was pointed out in the previous Section that the convergence rate obtained with a single enriched node (topological enrichment) leads to the same rate of convergence as the standard FEM, namely 1/3 in H^1 seminorm and 2/3 in relative error in strain energy. It has been shown by Laborde et al. [34] and Béchet et al. [37] that optimal convergence (rate of unity in the H^1
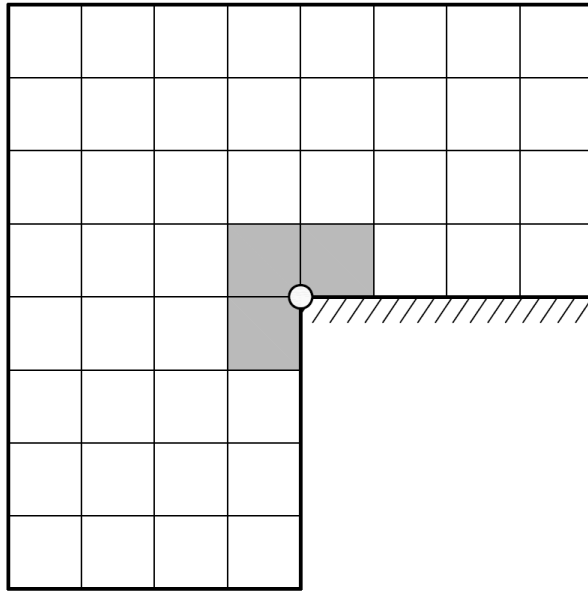
Figure 5: *L*-shaped domain problem with a single enriched node at re-entrant corner (topological enrichment).
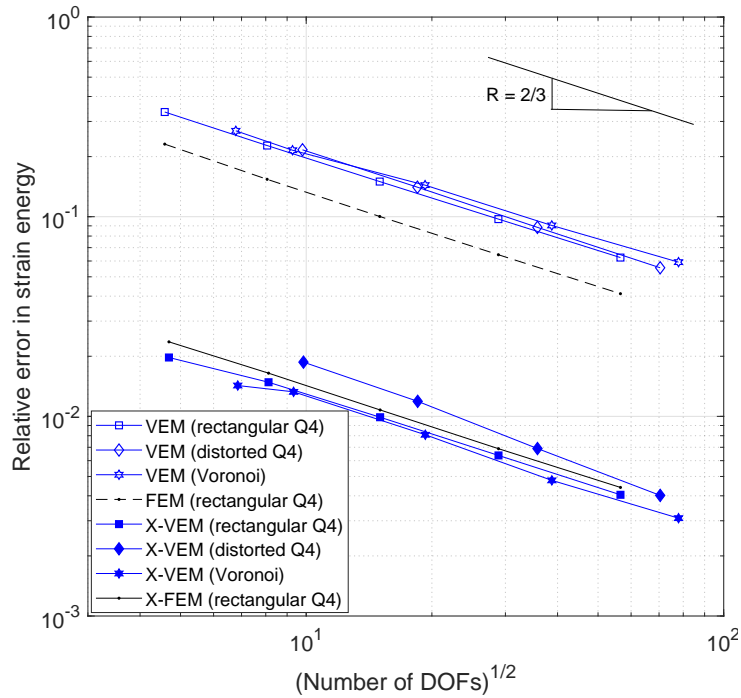
Figure 6: Convergence in terms of relative error in strain energy for the *L*-shaped domain problem where only the node at the re-entrant corner is enriched (topological enrichment). Comparisons are made with both the standard VEM and standard FEM/X-FEM (from [36]) on quadrilateral and polygonal meshes. All methods converge with a rate close to 2/3.

22
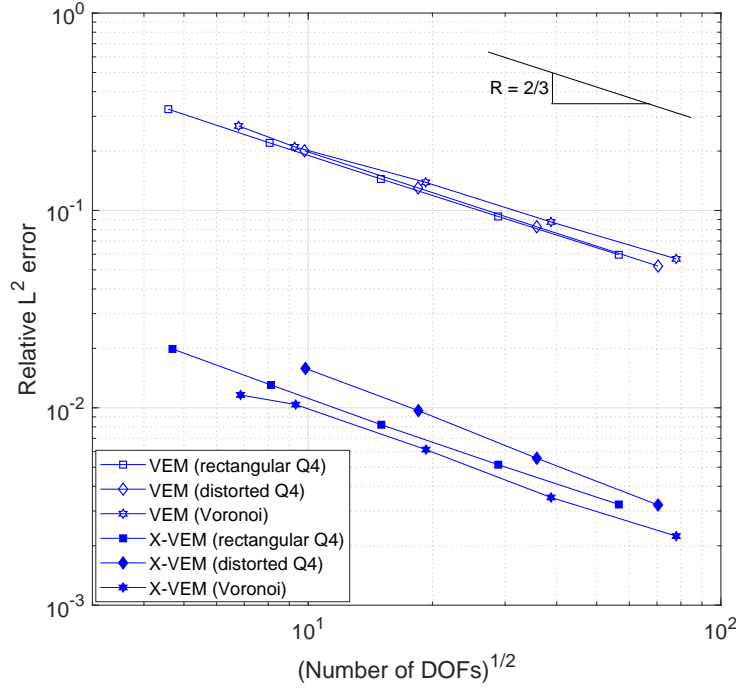
Figure 7: Convergence in terms of relative L^2 error for the L-shaped domain problem where only the node at the re-entrant corner is enriched (topological enrichment). Comparisons are made with the standard VEM on quadrilateral and polygonal meshes. All methods converge with a rate close to 2/3.
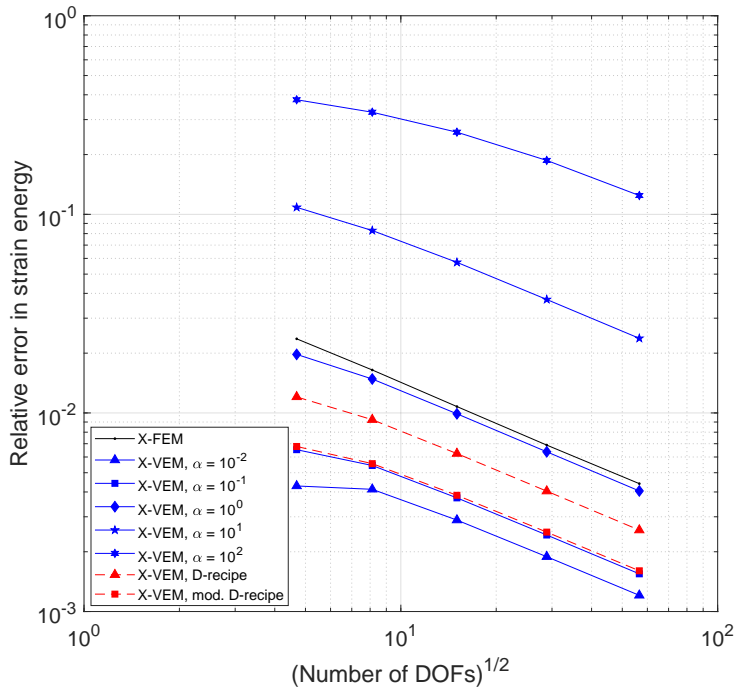
Figure 8: Sensitivity of the convergence to the stabilization parameter α for the L-shaped domain problem where only the node at the reentrant corner is enriched (topological enrichment) and comparison with diagonal stabilizations.

23
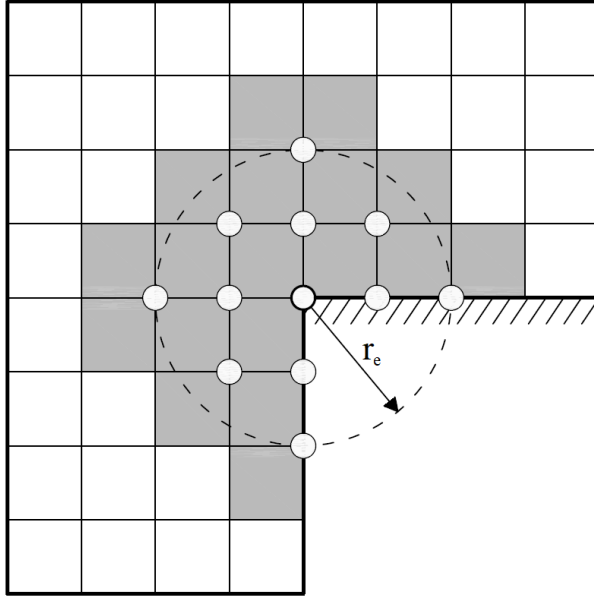
Figure 9: *L*-shaped domain problem where nodes that lie within the ball of radius $r_e = 0.5$ are enriched (geometric enrichment).

seminorm for crack problems) is recovered in the X-FEM if all nodes that lie within a fixed radius of the singularity are enriched. This strategy is referred to as *geometric enrichment*. The recovery of the optimal rate of convergence with geometric enrichment has been shown in many prior studies with the X-FEM for singular problems with cracks and corners.

To assess if the X-VEM can yield optimal convergence rates with geometric enrichment, we enrich all nodes that lie within a ball of radius $r_e = 0.5$ from the corner (see Fig. 9). Convergence plots for the relative errors in strain energy and L^2 norm are presented in Figs. 10 and 11, respectively, on quadrilateral as well as polygonal meshes. In both instances, the X-VEM convergence rates are close to 2, in agreement with theory. Finally, Fig. 12 depicts a comparison between convergence rates in strain energy for both topological and geometric enrichments for quadrilateral meshes and convex and non-convex polygonal meshes.

5.4. Discontinuous patch test

We are interested in evaluating the effectiveness and robustness of the X-VEM in the presence of discontinuities, and to this end, we devise a suitable patch test. As usual, the essential idea is to formulate a problem in which the exact solution lies in the discrete space and to verify if the extended virtual element approximation matches such a solution. For the problem at hand, we adapt the patch test first proposed by Dolbow and Devan [20] in finite strain elasticity to the present context of the Laplace problem that admits a piecewise linear solution. Consider the following Laplace problem of a membrane occupying the unit square domain Ω that is bisected by a discontinuity γ into two subdomains $\Omega^- = [0, 1] \times [0, 1/2]$ and $\Omega^+ = [0, 1] \times [1/2, 1]$, and subjected to zero Dirichlet boundary conditions along the edge $x = 0$ and discontinuous
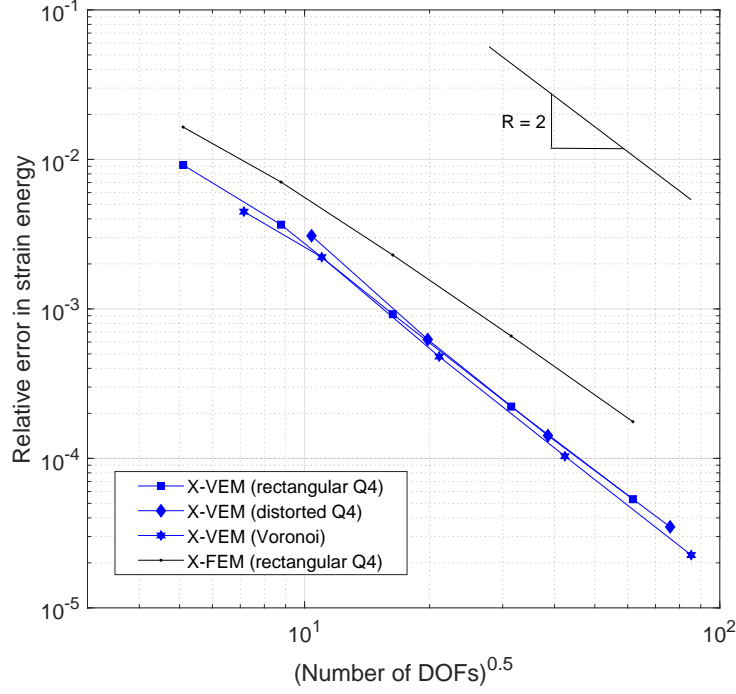
Figure 10: Convergence in terms of relative error in strain energy using geometric enrichment ($r_e = 0.5$). Extended virtual element computations are done with the elliptic projector Π_X^∇ on quadrilateral and polygonal meshes and are compared to both the standard VEM and the X-FEM from [36]. All methods converge with a rate close to 2.
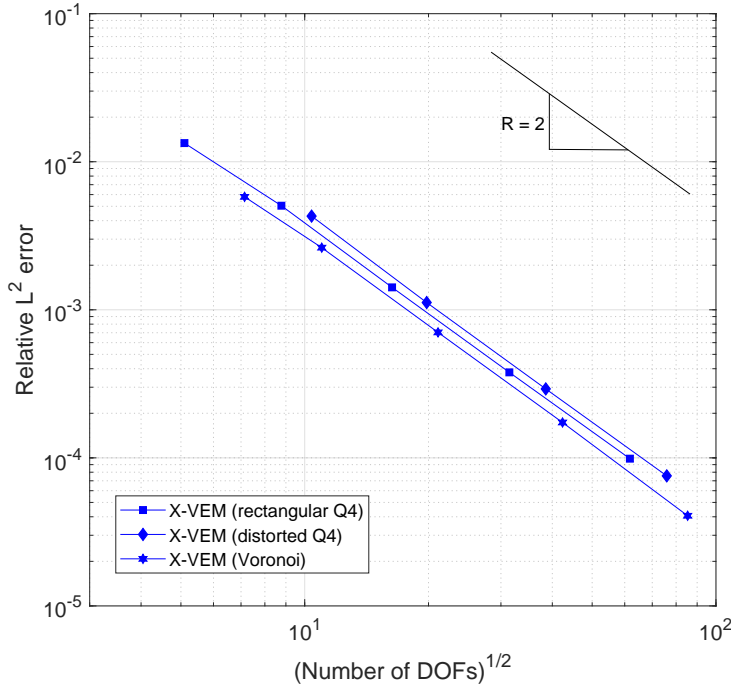
Figure 11: Convergence in terms of relative L^2 error using geometric enrichment ($r_e = 0.5$). Extended virtual element computations are done with the elliptic projector Π_X^∇ on quadrilateral and polygonal meshes. All methods converge with a rate close to 2.

25
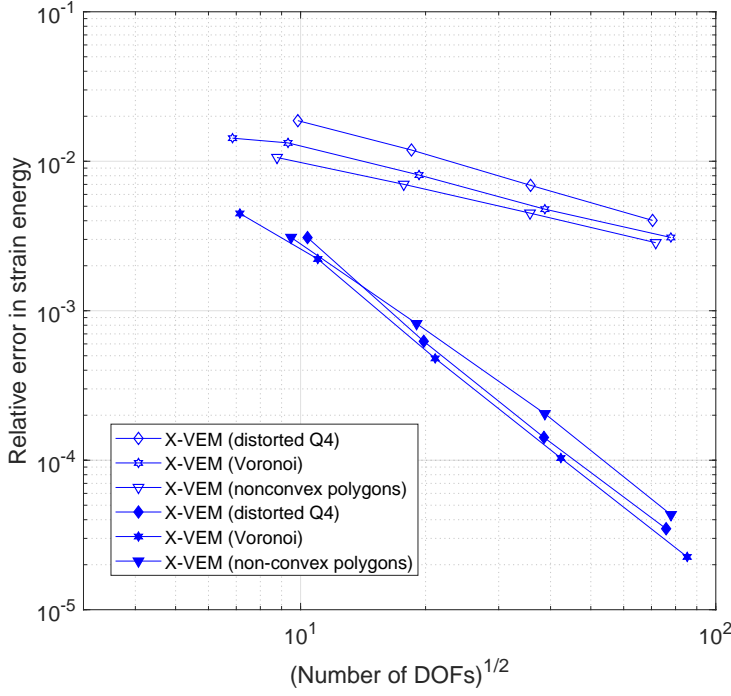
Figure 12: Comparison between convergence plots in terms of relative error in strain energy using topological enrichment (hollow markers) and geometric enrichment with $r_e = 0.5$ (solid markers). Extended virtual element computations are performed with the elliptic projector Π_X^∇ on distorted quadrilateral, polygonal and non-convex polygonal meshes.

Neumann boundary conditions along the edge $x = 1$ and horizontal edges:

$$\Delta u(x, y) = 0 \ \text{ in } \Omega \backslash \gamma, \tag{56a}$$

$$u(0, y) = 0, \tag{56b}$$

$$\frac{\partial u}{\partial x}(1, y) = \begin{cases} 1, & y \leq 1/2 \\ 2, & y > 1/2 \end{cases}, \tag{56c}$$

$$\frac{\partial u}{\partial y}(x, 0) = 0, \frac{\partial u}{\partial y}(x, 1) = 0. \tag{56d}$$

For this so-called discontinuous patch test, whose geometry and boundary conditions are shown in Fig. 13, the exact solution is the piecewise linear function

$$u(x, y) = \begin{cases} x, & \boldsymbol{x} \in \Omega^- \\ 2x, & \boldsymbol{x} \in \Omega^+ \end{cases}. \tag{57}$$

In agreement with expectations, the extended virtual element formulation proposed in Section 4.2, which uses distinct projector operators on the two subdomains that are formed by a crack that cuts the element, passes the patch test with errors on the order of machine precision.

5.5. Cracked membrane under mode III loading

We study the performance of the proposed X-VEM to model the behavior of a squared membrane that is partially cut into two parts by a central crack starting from one of the membrane

26
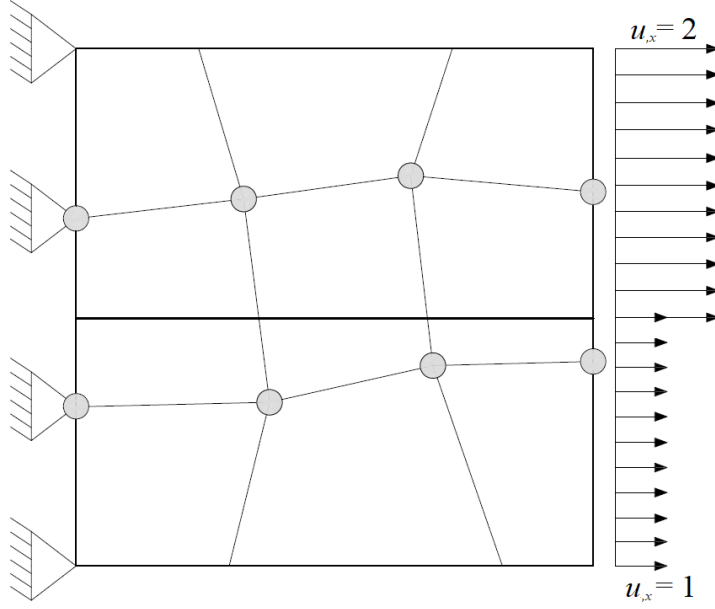
Figure 13: Geometry and loading conditions of the discontinuous patch test.

edges. These two parts are pulled in opposite directions through the application of out-of-plane displacements that are anti-symmetrical with respect to the membrane plane and linearly increasing from zero to ± 1 in the x direction, as illustrated in Fig. 14. The boundary of the membrane for $x \geq 0.6$ is clamped, i.e., zero transversal displacement are prescribed. Thus, the deformation of the membrane is characterized by a mode III opening displacement field. The determination of the displacement field of the cracked membrane is a Laplace problem (1), where the primal field u is its out-of-plane displacement. The cracked membrane, whose geometry is shown in Fig. 14, is assumed to be a unit square. We study the stability of the method on meshes with rectangular and polygonal elements. Two representative meshes are displayed in Fig. 15.

A series of simulations are performed on a sequence of refined rectangular and polygonal meshes. As in the previous problem, we adopt the stabilization (32), where the stabilization parameter α is set to 1. Diagonal stabilizations (see Section 4.1.2) are also investigated. Examples of deformed meshes are shown in Fig. 16. Convergence of the X-VEM on rectangular and polygonal meshes is studied, using a reference solution obtained with the X-FEM on an overkill mesh consisting of 409,600 square elements. The reference result for the strain energy is 0.575232. Fig. 17 shows the relative error in the strain energy with the X-VEM on quadrilateral and polygonal meshes. The rate of convergence of the X-VEM is consistent with that obtained with the X-FEM on quadrilateral meshes, but accuracy is superior with both quadrilateral and polygonal meshes.

The influence of the stabilization parameter α on the accuracy of the X-VEM on quadrilateral meshes is depicted in Fig. 18, along with the results provided by diagonal stabilizations introduced in Section 4.1.2. The choice $\alpha = 1$ in the X-VEM delivers results that are significantly more accurate with respect to the X-FEM, whereas increasing α leads to a progressive reduction in accuracy. However, convergence rate is maintained. Notably, among diagonal stabilizations, the *modified D-recipe* allows to realize the same accuracy as that obtained with the

27
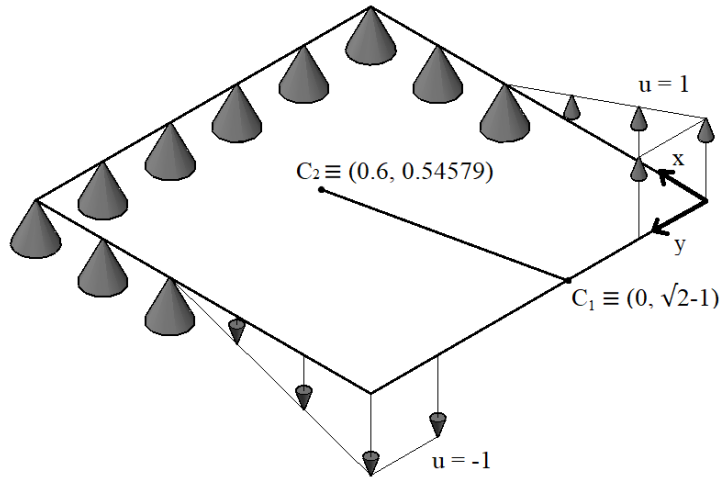
Figure 14: Geometry of the squared cracked membrane under prescribed boundary displacements along z-axis.

(a)

(b)
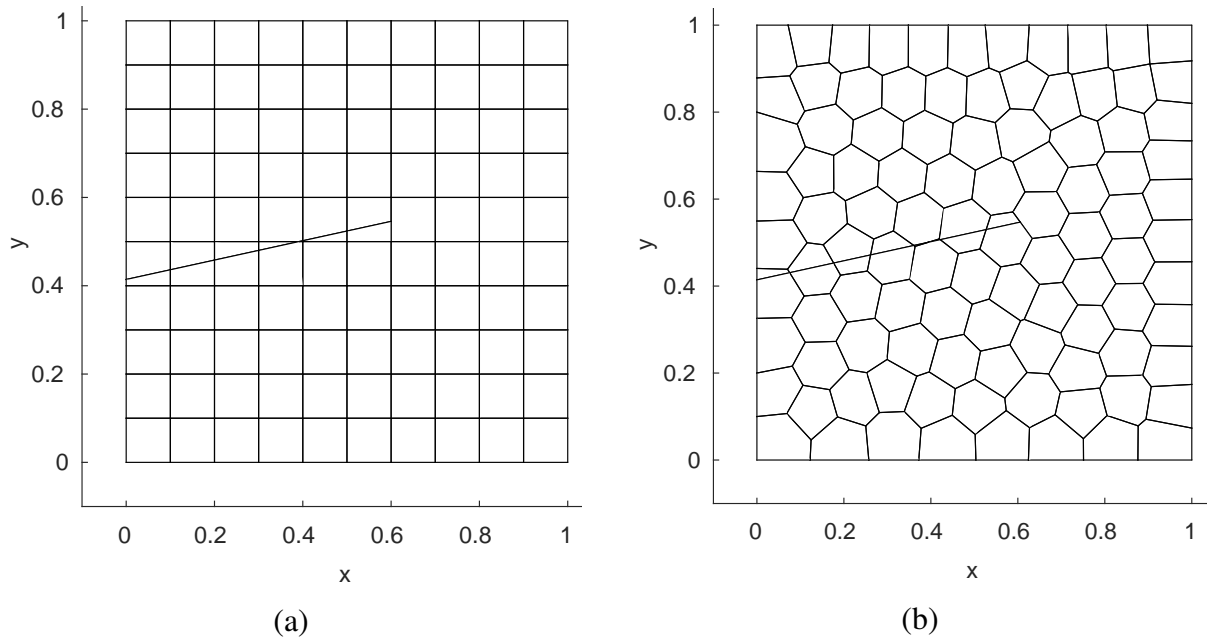
Figure 15: Representative meshes made of (a) square elements and (b) polygonal elements for the inclined crack problem.
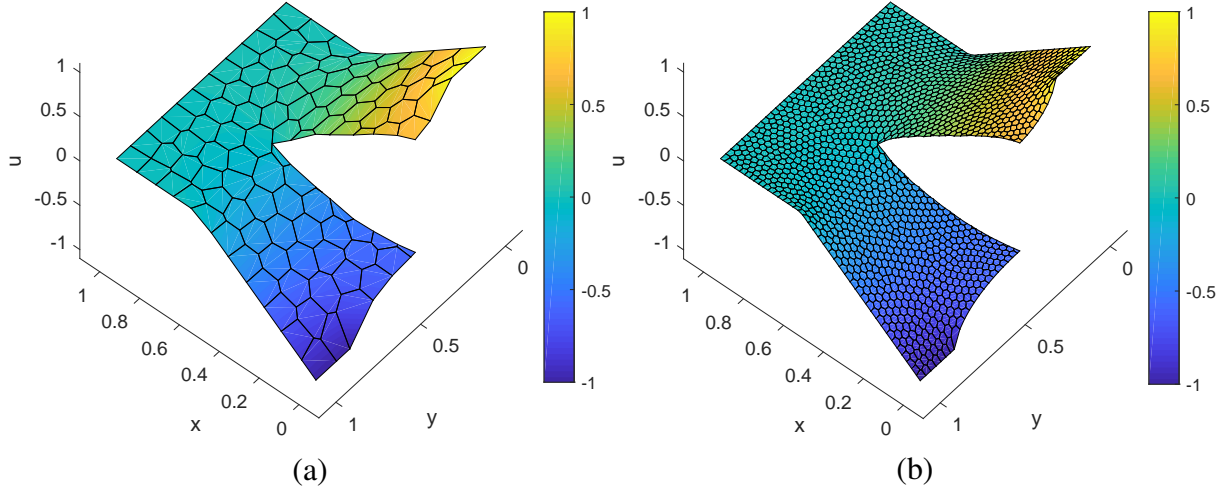
Figure 16: X-VEM contour plots of the deformed cracked membrane under mode III loading obtained from polygonal meshes with respectively (a) 100 elements and (b) 1600 elements.
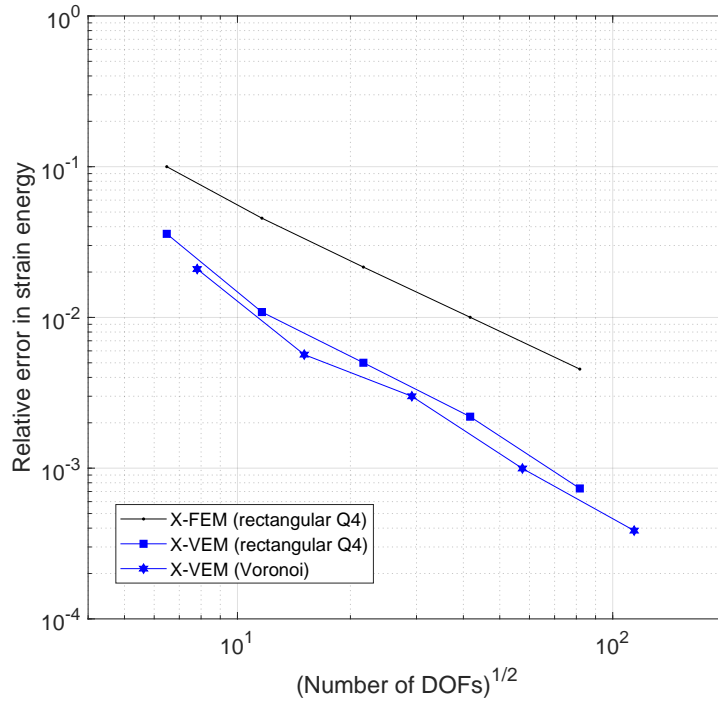
Figure 17: Convergence in terms of relative error in strain energy for the inclined crack problem using $\alpha = 1$.
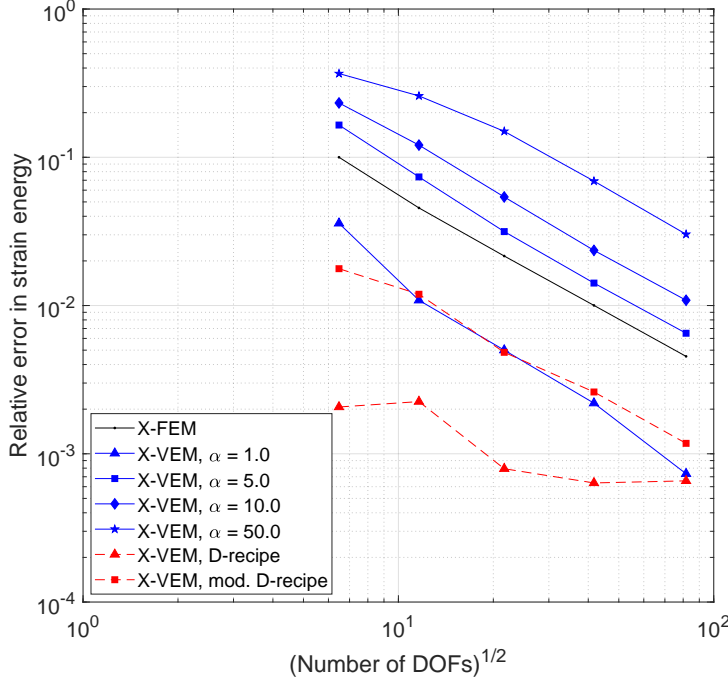
Figure 18: Influence of the stabilization parameter α on the relative error in the strain energy for the inclined crack problem and comparison with diagonal stabilizations.

stabilization in (33) ($\alpha = 1$) without the need for any tunable parameters. On the other hand, the standard *D-recipe* does not perform adequately for the problem under study. Overall, the proposed X-VEM for Laplace problems with discontinuities appears to be more accurate than the X-FEM on quadrilateral meshes, with optimal convergence rate, and furthermore, it has the flexibility of performing equally well on polygonal meshes.

Finally, similar to its finite element counterpart [38], the X-VEM with discontinuous enrichment can induce high condition numbers in the global stiffness matrix, which can lead to loss of accuracy when solving the algebraic system of linear equations. Poor matrix-conditioning arises when the discontinuity cuts an element E into two regions E^- and E^+ such that either E^- or E^+ is very small compared to E. This causes the approximation space of the enriched DOFs to be similar to the approximation space of non-enriched DOFs, leading to near linear dependence in the algebraic system of equations. Among the large number of methods for treating matrix ill-conditioning, a relatively simple technique is the use of a Jacobi (diagonal) preconditioner, which normalizes the diagonal of the stiffness matrix [39]. For low-order finite elements, this diagonal preconditioner suffices, though for higher-order finite element use of alternative stabilization techniques is needed to address the ill-conditioning [40]. The implementation of the preconditioner consists in applying the substitution $\boldsymbol{d} = \boldsymbol{D}\bar{\boldsymbol{d}}$ to the original linear system of equations $\boldsymbol{K}\boldsymbol{d} = \boldsymbol{f}$, where $\boldsymbol{D}$ is the inverse of the square root of the main diagonal of $\boldsymbol{K}$, i.e., $\boldsymbol{D} = \mathrm{diag}(\boldsymbol{K})^{-1/2}$. Then, we solve the system $(\boldsymbol{D}^T\boldsymbol{K}\boldsymbol{D})\bar{\boldsymbol{d}} = \boldsymbol{D}^T\boldsymbol{f}$, instead of the original system of equations. The diagonal entries of the modified stiffness matrix, $(\boldsymbol{D}^T\boldsymbol{K}\boldsymbol{D})$, are all ones.

In order to show the effect of preconditioner in the X-VEM and provide a viable solution to the ill-conditioning issue, we solve the mode III cracked membrane problem, discussed in the previous subsections, on a 5×5 mesh of square elements in the presence of a horizontal crack

30
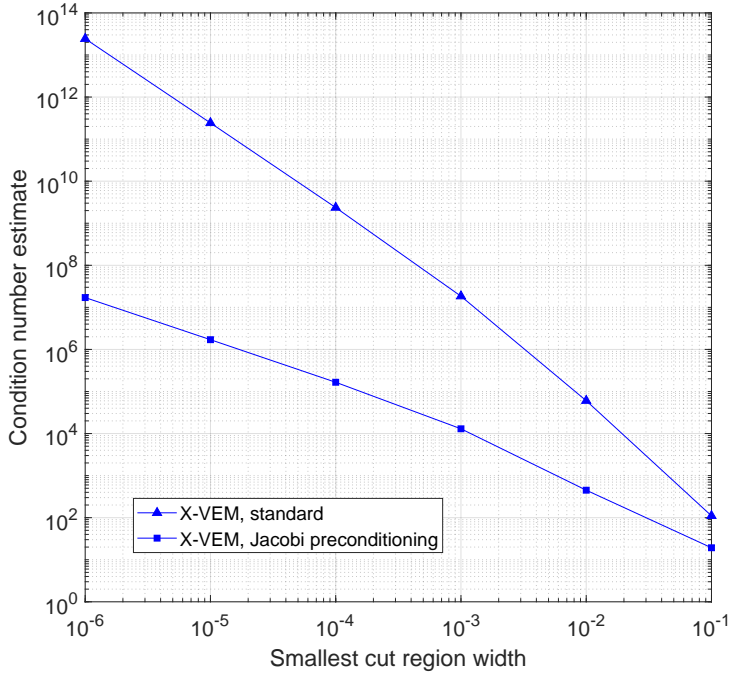
Figure 19: X-VEM stiffness matrix condition number for a mode III cracked membrane using the Jacobi preconditioner.

directed along the *x*-axis. The discontinuity is moved along the *y*-axis, so that each intersected element is cut into two rectangular regions with very different area, in order to intentionally provoke ill-conditioning in the global stiffness matrix. The width of the smallest region cut by the interface is used in Fig. 19 as a measure of the proximity of the interface to the element edge. As Fig. 19 illustrates, the preconditioner allows to considerably mitigate the issue of ill-conditioning.

6. Concluding remarks

We developed a stable and convergent extended virtual element method (coined as X-VEM) for the Laplace problem with vertex singularities and crack discontinuities. As in the X-FEM [3], we augmented the standard virtual element space with an additional contribution that consists of the product of virtual nodal basis (partition-of-unity) functions with enrichment functions. For the Laplace problem with a vertex singularity, we devised an extended projector that maps functions that lie in the extended virtual element space onto linear polynomials and the enrichment function. Crack discontinuities were modeled by tailoring the approach of Hansbo and Hansbo [18] to virtual elements, whereby each virtual shape function was decomposed as the sum of two discontinuous shape functions. The resulting stiffness matrix had a block-structure that was readily computed. We used the adaptive homogeneous numerical integration scheme devised in [7] and [8] to accurately and efficiently compute integrals with integrands that were weakly singular. We emphasize that in this integration scheme no element-partitioning is required. Once the element projection matrix was computed, well-established guidelines from the standard VEM [13] were followed to compute the element stabilization matrix. We also conducted a discontinuous patch test that verified the consistency of the proposed

31

method. Numerical experiments were performed on quadrilateral and polygonal meshes for the problem of an *L*-shaped domain with a corner singularity and the problem of a cracked membrane under mode III loading. For the *L*-shaped domain problem with geometric enrichment, the method delivered optimal rates of convergence in the L^2 norm and the strain energy. For the cracked membrane problem stable convergence in energy norm was observed, and better accuracy compared to the X-FEM was obtained. As in most studies on the VEM, the accuracy did depend on the choice of the stabilization term. We considered choices for the stabilization that were based on the trace of the consistency matrix (parameter α) and the diagonal entries of the consistency matrix (*D-recipe* with no tunable parameters) [26]. A modified version of the *D-recipe* stabilization yielded accurate results. Among potential topics for future work, we mention the extension of the present formulation to higher-order ($k \geq 2$) virtual element spaces and the application of the X-VEM to elastic and inelastic (cohesive models) fracture simulations in solid continua.

References

[1] J. M. Melenk, I. Babuška, The partition of unity finite element method: Basic theory and applications, Computer Methods in Applied Mechanics and Engineering 139 (1996) 289–314.

[2] I. Babuška, J. M. Melenk, The partition of unity method, International Journal for Numerical Methods in Engineering 40 (1997) 727–758.

[3] N. Moës, J. Dolbow, T. Belytschko, A finite element method for crack growth without remeshing, International Journal for Numerical Methods in Engineering 46 (1) (1999) 131–150.

[4] A. Tabarraei, N. Sukumar, Extended finite element method on polygonal and quadtree meshes, Computer Methods in Applied Mechanics and Engineering 197 (5) (2008) 425–438.

[5] A. Zamani, M. R. Eslami, Embedded interfaces by polytope FEM, International Journal for Numerical Methods in Engineering 88 (2011) 715–748.

[6] C. Song, E. T. Ooi, S. Natarajan, A review of the scaled boundary finite element method for two-dimensional linear elastic fracture mechanics, Engineering Fracture Mechanics 187 (2018) 45–73.

[7] E. B. Chin, J. B. Lasserre, N. Sukumar, Numerical integration of homogeneous functions on convex and nonconvex polygons and polyhedra, Computational Mechanics 56 (6) (2015) 967–981.

[8] E. B. Chin, J. B. Lasserre, N. Sukumar, Modeling crack discontinuities without element-partitioning in the extended finite element method, International Journal for Numerical Methods in Engineering 86 (11) (2017) 1021–1048.

[9] L. Beirão da Veiga, F. Brezzi, A. Cangiani, G. Manzini, L. D. Marini, A. Russo, Basic principles of virtual element methods, Mathematical Models & Methods in Applied Sciences 23 (2013) 119–214.

[10] P. Grisvard, Elliptic Problems in Nonsmooth Domains, Pitman Publishing, Inc, Boston, MA, 1985.

[11] I. Perugia, P. Pietra, A. Russo, A plane wave virtual element method for the Helmholtz problem, ESAIM: Mathematical Modelling and Numerical Analysis 50 (3) (2016) 783–808.

[12] B. Ahmad, A. Alsaedi, F. Brezzi, L. D. Marini, A. Russo, Equivalent projectors for virtual element methods, Computers & Mathematics with Applications 66 (2013) 376–391.

[13] L. Beirão da Veiga, F. Brezzi, L. D. Marini, A. Russo, The hitchhiker's guide to the virtual element method, Mathematical Models & Methods in Applied Sciences 24 (8) (2014) 1541–1573.

[14] M. F. Benedetto, S. Berrone, S. Pieraccini, S. Scialò, The virtual element method for discrete fracture network simulations, Computer Methods in Applied Mechanics and Engineering 280 (0) (2014) 135 – 156.

[15] M. F. Benedetto, S. Berrone, S. Scialò, A globally conforming method for solving flow in discrete fracture networks using the Virtual Element Method, Finite Elements in Analysis and Design 109 (2016) 23–36.

[16] M. F. Benedetto, A. A. Caggiano, G. Etse, Virtual elements and zero thickness interface-based approach for fracture analysis of heterogeneous materials, Computer Methods in Applied Mechanics and Engineering 338 (2018) 41–67.

[17] V. M. Nguyen-Thanh, X. Zhuang, H. Ngyyen-Xuan, T. Rabczuk, P. Wriggers, A Virtual Element Method for 2D linear elastic fracture analysis, Computer Methods in Applied Mechanics and Engineering 340 (2018) 366–395.

[18] A. Hansbo, P. Hansbo, A finite element method for the simulation of strong and weak discontinuities in solid mechanics, Computer Methods in Applied Mechanics and Engineering 193 (33-35) (2004) 3523–3540.

[19] P. M. A. Areias, T. Belytschko, A comment on the article 'A finite element method for simulation of strong and weak discontinuities in solid mechanics' by A. Hansbo and P. Hansbo [Comput. Methods Appl. Mech. Engrg. 193 (2004) 3523-3540], Computer Methods in Applied Mechanics and Engineering 195 (2006) 1275–1276.

[20] J. E. Dolbow, A. Devan, Enrichment of enhanced assumed strain approximations for representing strong discontinuities: addressing volumetric incompressibility and the discontinuous patch test, International Journal for Numerical Methods in Engineering 59 (1) (2004) 47–67.

[21] L. Beirão da Veiga, C. Lovadina, A. Russo, Stability analysis for the virtual element method, Mathematical Models & Methods in Applied Sciences 27 (13) (2017) 2557–2594.

[22] S. C. Brenner, Q. Guan, L.-Y. Sung, Some estimates for virtual element methods, Computational Methods in Applied Mathematics 17 (4) (2017) 553–574.

[23] F. Dassi, L. Mascotto, Exploring high-order three dimensional virtual elements: Bases and stabilizations, Computers & Mathematics with Applications 75 (9) (2018) 3379–3401.

[24] L. Mascotto, Ill-conditioning in the virtual element method: Stabilizations and bases, Numerical Methods for Partial Differential Equations 34 (4) (2018) 1258–1281.

[25] L. Beirão da Veiga, F. Brezzi, D. Marini, Virtual elements for linear elasticity problems, SIAM Journal on Numerical Analysis 51 (2) (2013) 794–812.

[26] L. Beirão da Veiga, F. Dassi, A. Russo, High-order virtual element method on polyhedral meshes, Computers and Mathematics with Applications 74 (2017) 1110–1122.

[27] N. Sukumar, J. E. Dolbow, N. Moës, Extended finite element method in computational fracture mechanics: a retrospective examination, International Journal of Fracture 196 (1) (2015) 189–206.

[28] E. Benvenuti, A. Chiozzi, G. Manzini, N. Sukumar, Numerical experiments with the extended virtual element method for the Laplace problem with strong discontinuities, Tech. Rep. LA-UR-18-23443, Los Alamos National Laboratory, Los Alamos, NM 87545, USA (2018).

[29] J. Duchon, Splines minimizing rotation-invariant semi-norms in Sobolev spaces, in: Constructive Theory of Functions of Several Variables, Vol. 571 of Lecture Notes in Mathematics, Springer-Verlag, Berlin, Germany, 1977, pp. 85–100.

[30] A. Sommariva, M. Vianello, Product Gauss cubature over polygons based on Green's integration formula, BIT Numerical Mathematics 47 (2) (2007) 441–453.

[31] T. Strouboulis, I. Babuška, K. Copps, The design and analysis of the generalized finite element method, Computer Methods in Applied Mechanics and Engineering 181 (1) (2000) 43–69.

[32] B. Szabó, I. Babuška, Finite Element Analysis, John Wiley & Sons, Inc., New York, N.Y., 1991.

[33] C. Talischi, G. Paulino, A. Pereira, F. Menezes, PolyMesher: a general-purpose mesh generator for polygonal elements written in Matlab, Structural and Multidisciplinary Optimization 45 (3) (2012) 309–328.

[34] P. Laborde, J. Pommier, Y. Renard, M. Salaün, High-order extended finite element method for cracked domains, International Journal for Numerical Methods in Engineering 64 (3) (2005) 354–381.

[35] L. Beirão da Veiga, A. Chernov, L. Mascotto, A. Russo, Exponential convergence of the hp virtual element method in presence of corner singularities, Numerische Mathematik 138 (2018) 581–613.

[36] S. E. Mousavi, N. Sukumar, Generalized Duffy transformation for integrating vertex singularities, Computational Mechanics 45 (2–3) (2010) 127–140.

[37] E. Béchet, H. Minnebo, N. Moës, B. Burgardt, Improved implementation and robustness study of the X-FEM for stress analysis around cracks, International Journal for Numerical Methods in Engineering 64 (8) (2005) 1033–1056.

[38] I. Babuška, U. Banerjee, K. Kergrene, Strongly stable generalized finite element method: Application to interface problems, Computer Methods in Applied Mechanics and Engineering 327 (2017) 58–92.

[39] C. Lehrenfeld, A. Reusken, Optimal preconditioners for Nitsche-XFEM discretizations of interface problems, Numerische Mathematik 135 (2) (2017) 313—332.

[40] E. B. Chin, N. Sukumar, Modeling curved interfaces without element-partitioning in the extended finite element method, International Journal for Numerical Methods in Engineering (2019) `doi:10.1002/nme.6150`.